In submission of S7Z – Master of Marine and Antarctic Science Research Component

Lithogenic particle flux to the subantarctic Southern Ocean: a multi-tracer estimate using sediment trap samples

by

Christopher D. Traill, BSc (Hons, UniMelb)*

Supervised by Dr. Morgane M.G. Perron, Prof. Zanna Chase and Prof. Andrew R. Bowie

A thesis submitted in partial fulfilment of the requirements of the Master of Marine and Antarctic Science (S7Z) at the Institute for Marine and Antarctic Studies (IMAS), University of Tasmania (May, 2021)

* christopher.traill@utas.edu.au. Institute for Marine and Antarctic Studies, University of Tasmania, 20 Castray Esplanade, Battery Point TAS 7004.

Declaration of Authorship

The Author asserts that this thesis contains no material which has been accepted for the award of any other degree or diploma in any tertiary institution, and that, to the best of the candidate's knowledge and belief, the thesis contains no material previously published or written by another person, except where due reference is made in the text of the thesis.

Christopher David Traill

Date: 14/05/2021

Abstract

The delivery of lithogenic material from atmospheric dust to remote regions of the Southern Ocean is thought to be a key source of micronutrients, particularly iron, essential for phytoplankton. Here, we present a time series of lithogenic flux estimates from 2010 to 2019 using sinking particles collected by sediment traps at 1000m at the Southern Ocean Time Series mooring station in the subantarctic Southern Ocean. Lithogenic flux estimates were made based on aluminium, titanium, iron and thorium concentration in sinking particles and showed good agreement with one another. A multi-tracer flux estimate was calculated using an average of all individual tracer flux estimates in order to reduce biases associated with each element's reactivity in seawater. This mean lithogenic flux exhibited a strong seasonality, with two peaks in late spring and in summer. The magnitude of our multi-tracer lithogenic flux was comparable to previous sediment trap-based fluxes reported in the Southern Ocean and to ^{230}Th-normalised lithogenic fluxes from core-top sediments at the same study location. A lack of lithogenic tracer enrichment in our samples compared to the average upper continental crust values indicated that lithogenic material dominates iron supply in this region. Sinking particle samples from SOTS showed similar Fe enrichment to aerosols collected over southern marine regions around Australia, suggesting that Australian dust may be the primary lithogenic source to SOTS sinking particles. Evidence of lead (Pb) enrichment in sediment trap samples at 1000m highlighted a non-negligible contribution from anthropogenic particles in SOTS sediments, the later source which could represent a secondary Fe supply to the samples. Therefore, we concluded that aeolian emissions from Australia likely compose the primary source of lithogenic particles to SOTS subantarctic Southern Ocean 1000m-deep waters. This hypothesis was further supported by maximum lithogenic particle flux at 1000m depth in late spring preceded by seasonal atmospheric aerosol loading from aerosol optical depth and satellite reanalysis modelled dust deposition maxima that occurred during the Australian dust storm season in spring across the study period.

While carbon export at 1000m showed good correlation with surface chlorophyll concentrations at SOTS across the study period, a lack of linear relationship between lithogenic fluxes at 1000m and productivity leaves the link between marine productivity and 1000m-deep sinking particles in this subantarctic region of the Southern Ocean unclear.

Acknowledgments

The author wishes to acknowledge and give thanks for the assistance of: Morgane Perron, Zanna Chase and Andrew Bowie (IMAS/UTAS) and for their contributions to project design, interpretation of results, editing of manuscript materials and pastoral support; Axel Durand for his knowledge and experience in sediment digestion; the assistance and experience of Ashley Townsend (UTAS CSL) for ICP-MS data acquisition and data interpretation constraints; Cathryn Wynn-Edwards (AAPP/CSIRO) for her excellent previous work on SOTS sediment trap samples, management and compilation of data, guidance, and conceptual consultation; IMAS Sediment Laboratory team for their support and analytical critique of results.

The author wishes to gratefully acknowledge project funding provided by the Australian Research Council Discovery Project grant scheme. Grant reference: DP190103504

Table of Contents

List of Figures

List of Tables

List of Equations

1. Introduction

1.1 – Role of the Southern Ocean in atmospheric carbon dioxide uptake

The Southern Ocean plays a critical role in the regulation of global climate by acting as an interface between atmospheric carbon dioxide (CO_2) and carbon storage in the deep ocean (Sabine et al., 2004; Gruber et al., 2009; Shadwick et al., 2015; Pardo et al., 2017). The ventilation of natural (pre-industrial) CO_2 from carbon rich deep waters driven by the global thermohaline overturning circulation (Marshall and Speer, 2012), is balanced by the fixation of atmospheric CO_2 by primary productivity into organic matter (Lauderdale et al., 2017). The subsequent transport of sequestered carbon to the deep ocean through detritus and excreted particles is termed the biological pump (Marinov et al., 2006; Hauck et al., 2015; Lauderdale et al., 2017). Regional variations in the balance between uptake and outgassing of CO_2 generate uncertainty in Southern Ocean carbon flux understanding (Marinov et al., 2006; Gruber et al., 2009; Hauck et al., 2015; Shadwick et al., 2015). The Southern Ocean's ability to sequester carbon from the atmosphere via primary productivity is therefore an important factor in quantifying carbon budgets in this globally significant region. Moreover, with already a significant (~40%) proportion of anthropogenic CO_2 stored in the Southern Ocean (Khatiwala et al., 2009)**,** understanding the efficiency of the biological pump is an integral part in predicting future climate scenarios.

1.2 – Iron limitation in the Southern Ocean

The Southern Ocean is characterised as a high nutrient low chlorophyll (HNLC) oceanic region, where excess macronutrient levels indicate that the efficiency of the biological pump is limited by restriction in the growth of primary producers (Hauck et al., 2015). Early work by Martin et al. (1990) suggested that phytoplankton growth in HNLC regions like the Southern Ocean was limited by the scarcity of the essential trace nutrient iron (Fe). This hypothesis was further confirmed by subsequent mesoscale iron fertilisation experiments (Boyd et al., 2007), prompting a quest to understand iron sources to the ocean (Tagliabue et al., 2014) and mechanisms governing its biogeochemical cycle (Tagliabue et al., 2017). Other trace elements (TEs) are essential to phytoplankton, including zinc (Zn), manganese (Mn), nickel (Ni), copper (Cu), cobalt (Co) and cadmium (Cd) (Twining and Baines, 2013), which may co-limit phytoplankton growth at low oceanic concentration. In particular, iron and manganese colimitation was observed in some areas of the Southern Ocean (Middag et al., 2013; Browning

et al., 2014). Since the dissolved fraction of trace metals in seawater denotes the bioavailability of trace nutrients, the solubility of trace metals delivered to the ocean may also be a limiting factor to phytoplankton growth (Twining and Baines, 2013). Investigating the sources, delivery pathway, and uptake of iron and other trace metals in seawater is key to better constraining the link between biogeochemical cycles and marine primary productivity, as well as their impact on the oceanic carbon budget and climate change (Boyd et al., 2007; Boyd and Ellwood, 2010; Smetacek et al., 2012; Tagliabue et al., 2017).

1.3 – Sources of trace metals to the open ocean

In remote open ocean regions, TE supply to surface seawater from sediments is supplemented by atmospheric deposition of mineral dust, anthropogenic aerosols and biomass burning (Duce and Tindale, 1991; Jickells et al., 2005; Mahowald et al., 2005; Luo et al., 2008). Around 25% of global dust emissions (1490 – 1814 Mt yr^{-1}) are deposited to the ocean annually (Shao et al., 2011). Much of this deposition occurs in the northern hemisphere due to the presence of large deserts and arid regions of North Africa, the Middle East and Asia (Maher et al., 2010). In the Southern Ocean however, only three major land masses – Australia, South America and Southern Africa – act as dust source regions (Shao et al., 2011). Despite dust emission in the Southern hemisphere being smaller than north of the equator (Maher et al., 2010), the Fe-limited nature of the vast Southern Ocean may result in a disproportionate impact of TE delivery from mineral dusts on ocean productivity in this region (Mahowald et al., 2005; Myriokefalitakis et al., 2018). A better understanding of mineral dust delivery to the Southern Ocean is therefore essential in order to constrain lithogenic inputs and biogeochemical cycles in this region (Boyd et al., 2010). To this effect, sources of TE delivery to the ocean, such as lithogenic inputs from mineral dust, can be identified using tracers of crustal material including Fe, aluminium (Al), titanium (Ti) and thorium (Th) (Ohnemus and Lam, 2015; Anderson et al., 2016).

In addition to lithogenic sources, TEs may be supplied to the ocean by anthropogenic aerosols (Pacyna and Pacyna, 2001; Sholkovitz et al., 2009; Baker et al., 2016). These latter aerosols are produced by fossil fuel emissions such as coal burning, industry, commercial shipping and transport emissions (Pacnya and Pacnya, 2001). Combustion aerosols are of particular interest as they were demonstrated to contain a higher fraction of soluble iron compared to mineral dust (Sholkovitz et al., 2009; Ito et al., 2019). This is significant for HNLC regions, since increased input of bioavailable iron to phytoplankton may largely stimulate primary productivity

(Sholkovitz et al., 2012; Ito et al., 2020b). Thus, in the context of high anthropogenic emissions to the atmosphere, atmospheric source apportionment is important to assess the impact of atmospheric deposition of soluble TEs on ocean productivity and subsequently on oceanic carbon drawdown (Ito et al., 2019; Ito et al., 2020b). Chemical tracers such as vanadium (V) and lead (Pb) (Sholkovitz et al., 2009; Eyring et al., 2010; Shelley et al., 2017b) are valuable tools to trace aerosols emitted by fuel combustion (Perron et al., 2020a). In particular, relatively stable and small Pb content in the upper continental crust (UCC) (Rudnick and Gao, 2003) make Pb enrichment in marine particles a strong indicator of anthropogenic 'contamination' (Shelley et al., 2017b; Buck et al., 2019).

1.4 – TE supply to the ocean from models vs. observations

Previous efforts to quantify modern atmospheric TE deposition to the Southern Ocean have largely relied on modelled dust deposition (Li et al., 2008; Boyd et al., 2010), due to the difficulty in obtaining direct observations in this remote ocean region (Bullard et al., 2016; Myriokefalitakis et al., 2018). The parameterisation of northern hemisphere dust emission, transport and deposition in the tuning of models has previously been implicated in over estimation of dust deposition to the Southern Ocean (Bowie et al., 2009; Albani et al., 2014; Myriokefalitakis et al., 2018; Ito et al., 2020a). Atmospheric deposition observations in the Southern Ocean are thus essential for improved Southern Hemisphere dust modelling (Albani et al., 2014; Myriokefalitakis et al., 2018). Although atmospheric deposition estimates from at-sea collection of aerosol samples (Bowie et al., 2009; Perron et al., 2020a; Strzelec et al., 2020) are key to understanding the geochemistry and solubility of aeolian TEs, these samples only integrate atmospheric measurements over a few days (Anderson et al., 2016). Moreover, the short time scale of oceanographic campaigns (several weeks) does not allow an accurate representation of either highly episodic major weather events (dust and fire emission) or seasonal and inter-annual dust deposition trends from aerosol sampling alone (Mahowald et al., 2009; Jickells and Moore, 2015). Finally, the extreme weather conditions and remoteness of the Southern Ocean prevent the practical installation of time series aerosol sampling devices outside of oceanographic expeditions.

1.5 – Dust deposition estimation using lithogenic tracers

To obtain estimates of dust deposition to the ocean over longer time scales, tracers of lithogenic material in sub-surface particles (sinking and benthic surface sediments) and dissolved tracer concentrations can be used as a proxy for estimating dust deposition (Anderson et al., 2016).

In oceanic regions where lateral inputs of advected hemipelagic sediment contribution to particle flux is negligible or corrected for, the lithogenic flux derived from sub-surface particles can be equated to dust deposition (Anderson et al., 2016). Lithogenic flux estimates on the scale of 1-3 years can be estimated from sinking particles using the ^{230}Th-normalised flux of ^{232}Th (Francois et al., 2004), ^{230}Th-based particle sinking rates and ^{232}Th particle concentrations (Anderson et al., 2016), or particle Al, Fe and Ti concentrations in combination with models (Ohnemus and Lam, 2015). The ^{230}Th-normalised flux of ^{232}Th from surface sediments can be used to estimate lithogenic flux over much longer periods (several hundred years to millennia) due to sediment accrual over time (Francois et al., 2004; Kienast et al., 2016). Dissolved concentrations of lithogenic tracers including Al and ^{232}Th can provide estimates of lithogenic flux at 1-5 year time scales depending on the solubility of aerosols delivered to the ocean and the residence time of dissolved tracers (Anderson et al., 2016). Sediment traps measure the flux of sinking particles through the water column during deployments lasting up to 18 months, with estimates of lithogenic flux derived from the concentration of lithogenic tracers (Al, Ti, Fe and Th) in collected particles or by mass balance. While these methods all contain inherent biases of varying magnitude, the combined use of multiple methods and tracers for dust flux estimation was recommended in order to provide more reliable estimates by identifying inconsistencies between methods (Anderson et al., 2016).

1.6 – Sediment traps and lithogenic particle flux

Sediment traps are useful tools to collect sinking marine particles in remote ocean settings, as they allow autonomous and continuous high-resolution sample collection (minutes to weeks), capable of capturing seasonal and annual variability in particle fluxes. Nevertheless, quantitative flux estimates from sediment traps are subjected to biases. Under-collection of sinking particles may occur when turbulence at the trap mouth and tilting of the trap are induced by hydrodynamic interactions between the trap and ocean currents (Yu et al., 2001; Buesseler et al., 2007; Chiswell and Nodder, 2015). Collected particle solubilisation can selectively alter particle composition reducing particle mass flux calculations (Antia, 2005; Buesseler et al., 2007). Zooplankton swimmers may actively enter traps, especially at shallower depths, disturbing the passive flux of sinking particles or becoming trapped and perturbing particle component concentrations (Yu et al., 2001; Buesseler et al., 2007). Despite these inherent biases, sediment traps can be set up to minimise these effects and currently provide the best

direct year-round measurements of particle flux and export production in remote ocean settings (Wynn-Edwards et al., 2020).

The calculation of lithogenic fluxes using sediment trap material has principally relied on either the measurement of lithogenic tracers in particles collected, or by the calculation of the mass balance of particle constituent components collected. In the Southern Ocean, sinking sediment Al concentrations have been used previously to proxy lithogenic flux, where the total lithogenic material is inferred using the crustal concentration of Al (Trull et al., 2001; Nodder et al., 2016). Lithogenic fluxes from sediment traps may also be indirectly estimated by subtracting individual measurements of components of the total mass flux, typically inorganic carbon, organic matter and biogenic opal, providing a residual lithogenic component estimate by mass balance (Wefer and Fischer, 1993). However, this method relies on assumptions on organic matter composition in samples and does not account for authigenic mineral contributions to total particle mass which may cause uncertainty. Since the use of lithogenic tracers and sediment trap particles relies on the refractory nature of the tracer used, variations in the reactivity of lithogenic tracers (such as Al, e.g. Dymond et al. (1997)) may generate uncertainty. The combination of multiple tracers (Al, Ti, Fe and Th) may provide more robust estimates of lithogenic flux variability by reducing inconsistencies due to tracer specific biases. Additionally, the analysis of anthropogenic tracers (V, Pb) can used to assess anthropogenic contributions of TE delivery to the ocean.

1.7 – Aims

The estimation of lithogenic particle fluxes in the Southern Ocean using sediment traps is made possible by the Southern Ocean Time-Series station, located in the subantarctic (SAZ) Southern Ocean, south of Tasmania, Australia (47°S, 142°E). The SAZ comprises waters between the sub-tropical front and subantarctic front (Figure 1). The SOTS location is considered broadly representative of Indian/Australian sector SAZ waters from ~90 to ~145°E (Trull et al., 2001; Shadwick et al., 2015; Trull et al., 2019). With Australia the largest dust contributor in the southern hemisphere (Shao et al., 2011), remote ocean observations from SOTS south of Australia presents a unique setting to sample atmospheric deposition of lithogenic material to the Southern Ocean.

Here, a time series of lithogenic flux estimates is presented based on the analysis of sediment trap samples collected at 1000m depth at SOTS (47°S, 142°E) between 2010 and 2019. Sediment digestion by a cocktail of strong acids was used to completely extract trace metals of interest in this study. Principally Al, Ti, Fe and Th concentrations in sediments were used to estimate lithogenic flux and averaged to reduce flux estimate biases associated with variations in metal reactivity in the marine environment. The estimation of lithogenic particle fluxes from sediment traps contributes to much needed observations of TE supply and dust deposition to the Southern Ocean, which are currently limited (Bullard et al., 2016; Myriokefalitakis et al., 2018).

Through our obtained average lithogenic particle flux time series, we aim to assess:

1) The variability and sources of crustal material downward flux in the SAZ between 2010 and 2019
2) The use of such estimates as a proxy for aeolian deposition of mineral dust at SOTS
3) Lithogenic particle interactions with components of the total mass flux in particles obtained at SOTS 2010-2019 and remotely sensed productivity signals.

2. Methods

2.1 – Study design and location

This study uses sinking marine particles collected at the Southern Ocean Time Series (SOTS) mooring station established in 1997. The SOTS moorings are located at 47°S 142°E, about 500 km southwest of Tasmania (Australia) in 4500m water depth. This open ocean location is situated at the convergence of nutrient-poor subtropical waters to the north and high nutrient low chlorophyll waters of the Southern Ocean to the South (Figure 1). SOTS is comprised of a deep ocean sediment trap mooring (SAZ), a surface biogeochemistry mooring (Pulse, intermittent deployment) and an air-sea flux mooring (SOFS). SOTS therefore provides continuous and valuable insights into a range of physical and biogeochemical processes in subantarctic waters over time (Shadwick et al., 2015; Trull et al., 2019; Wynn-Edwards et al., 2020). Sinking marine sediments have been collected at a range of depths at SOTS, using McLane Parflux conical sediment traps, almost continuously since 1997, affording nearly two decades of archived sinking particle samples.

Here, we use a selection of <1mm size fraction sediment samples collected between 2010 and 2019 at 1000m depth. Samples were selected according to the consistency of sampling during mooring deployments, as multiple gaps exist in the sampling activity due to ship availability, funding or mooring damage/loss. The 1000m depth sediment trap series was selected in preference to SOTS deep traps at 2000m and 3800m due to its proximity to the ocean surface. In order to effectively determine mineral dust inputs of lithogenic particles arriving at depth, this relatively shallower trap deployment avoids sub-surface lithogenic inputs from re-suspended sediments (Buesseler et al., 2007) or hydrothermal sources (Tagliabue et al., 2010). Trap deployment at 1000m depth reduces many of the uncertainties of sediment trapping, since greater trapping biases are generally observed in the upper 1000m largely due to faster currents (Buesseler et al., 2007). At SOTS, the 1000m trap depth is sufficiently deep to avoid turbulence from the winter mixed layer that reaches 500m depth (Rintoul and Trull, 2001; Trull et al., 2019).

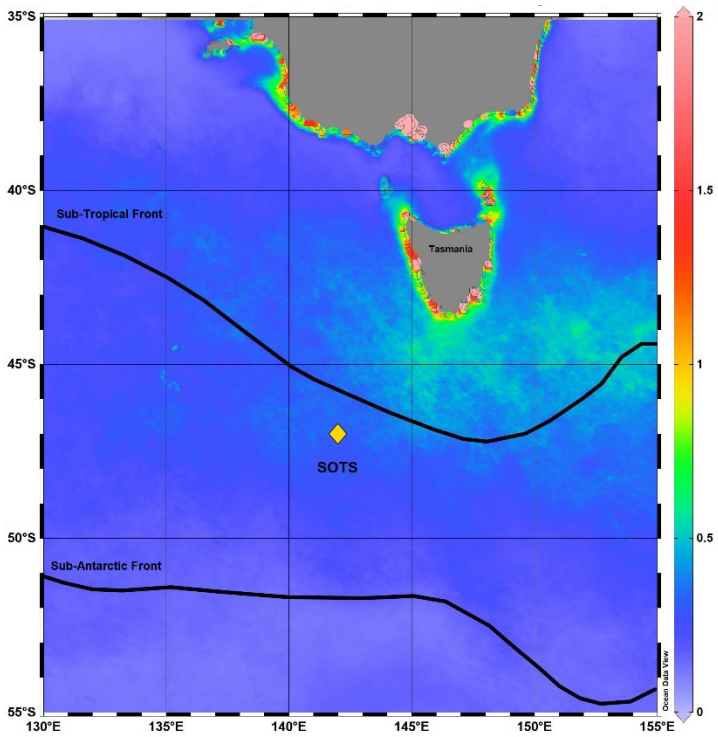

Figure 1. The SOTS deep water mooring station at 47°S 142°E (yellow diamond) is located at the interface between temperate sub-tropical waters and cool subantarctic waters of the Antarctic Circumpolar Current. Solid lines denote approximate front locations. Shading denotes satellite (MODIS-Aqua) mean surface chlorophyll concentration (mg m^{-3}) for December, January, and February 2011-2018.

Detailed information on the SOTS moorings and the design of sediment traps can be found in Trull et al. (2001), Wynn-Edwards et al. (2020) and in CSIRO-MNF technical reports (and references therein).

2.2 – Sample collection

Full details on sediment trap sample handling and processing, including quality assurance and control procedures, can be found in Wynn-Edwards et al. (2020).

Sinking marine sediments were collected in McLane Parflux Mark-78H 21-cup sediment traps of 0.5 m^2 effective collection area (Figure 2). Traps were fitted with a 2.5 cm-grid honeycomb baffle to exclude large swimmers. Each cup collected sediment samples over a period of 15-17 days (duration dependent on deployment), thus each cup represents a single sample point. Cups (sampling bottles in Figure 2) were filled with a high density brine solution consisting of 0.8 um GF/F-filtered seawater collected at the SOTS, with added NaCl (5 g L^{-1}) to increase density, reduce re-sedimentation and improve particle retention, $Na_2[B_4O_5(OH)_4]\cdot 8H_2O$ (borax; 2 g L^{-1}) to buffer pH and reduce carbonate dissolution, $SrCl_2\cdot 6H_2O$ (0.22 g L^{-1}) to preserve $SrSO_4$ acantharians, and $HgCl_2$ (3 g L^{-1}) to act as biocide. Cups displaying a noticeable foul odour were spiked with an additional 100 µL of $HgCl_2$ (saturated solution). The <1 mm size fraction was obtained by passing the contents of each cup through a 1 mm nylon sieve rinsed with a stream of 0.8 µm GF/F filtered seawater buffered with borax (1 g L^{-1}). This material was split into 10 sub-samples using a McLane wet sample divider (McLane, WSD-10). Three sub-samples were archived, and the remaining seven were re-combined and filtered onto a 0.4 µm 47 mm polycarbonate membrane filter. The filter was rinsed with ultra-high purity water (UHPW) to remove remnant brine salts (preventing the need for salt correction in dry sample mass) and dried over several days at 60°C until constant weight was obtained. Dried samples were scraped from the filter and ground using a mortar and pestle, accurately weighed and stored in scintillation vials. Total mass

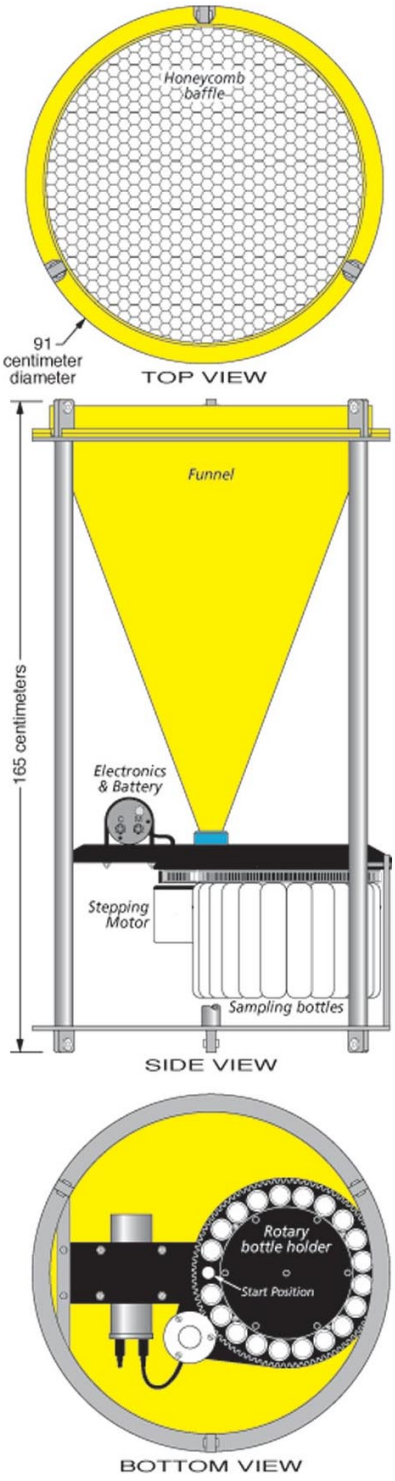

Figure 2. McLane Parflux 21-cup sediment trap schematic. Effective catchment area (baffled area) is 0.5 m^2. Image: Woods Hole Oceanographic Institute

flux (TMF) for each sample was calculated following Equation 1, resulting in an average mass flux over the duration of each cup sample collection.

$$TMF = \frac{\frac{10}{7} \times (\text{dry sample mass})}{0.5 \times (\text{cup collection duration in days})} \quad \textbf{(1)}$$

Mass flux data was not corrected for trapping efficiency owing to lack of consensus on how to apply current speed and trap tilt to hydrodynamic processes impacting trapping of a broad size range of particles (Buesseler et al., 2007; Chiswell and Nodder, 2015; Wynn-Edwards et al., 2020; see §4.1). Total mass fluxes, biogeochemical component analyses and sample quality controls were conducted by Wynn-Edwards et al. (2020) and references therein. Open access data is available from the Australian Ocean Data Network portal (https://portal.aodn.org.au/).

2.3 – Sample preparation

2.3.1 – Sample selection

For this study, archive samples of <1 mm size fraction dried sinking marine sediment collected at SOTS at 1000m depth were used. Archived samples were selected in order to generate minimal gaps in the time-series, with preference given to data covering complete years/seasons. Due to chemical safety, time and practical constraints, all samples, references and blanks were digested in batches of 22 to 48 samples, with a total of 4 batches, resulting in a total of 124 SOTS samples being analysed.

Reference materials used included:

- BCR-414 plankton certified reference sediment (European commission – Joint Research Centre, Geel, Belgium)
- CROCCA-2S TT1811-MC45 Indian Ocean surface sediment, in house reference
- IN2018_V02_KC07 0cm sediment core sample from SOTS site.

Reference materials together with archive SOTS samples were dried again at 60°C for a minimum of 48 hours prior to analysis to remove potential moisture accrued during storage. Dry samples were left to cool and weighed (~50 mg nominal mass) directly into acid-washed Teflon PFA vials (Savillex 15 mL, see cleaning procedure below). At least two procedural blanks were included in each digestion batch. All sample handling and processing was undertaken in a ducted laminar flow hood (HEPA-100 class) following GEOTRACES

guidelines on trace metal clean techniques (Cutter et al., 2017) to prevent sample contamination. Distilled nitric (HNO_3) and hydrochloric (HCl) acids were produced in house from instrument quality acids (IQ grade, SEASTAR™, Sidney, BC, Canada) using a Savillex DST-1000 Acid purification system 100V (Eden Prairie, Minnesota, USA). Hydrofluoric (HF) and perchloric ($HClO_4$) acids were ultra-pure baseline quality (SEASTAR BASELINE™).

2.3.2 – Vial cleaning procedure

Vials were cleaned following GEOTRACES guidelines for sampling and sample handling (Cutter et al., 2017). Vials and lids were rinsed with ultra-high purity water (UHPW) (x3) prior to soaking in a 2% Decon-90 solution for 1 week. Vials were then placed in a bath of dilute HNO_3 (~3 M final concentration) and heated at 60°C for 1 week. Vials and lids were submerged again in diluted HCl (~2 M final concentration) and heated at 60°C for 1 week. Between each cleaning step, vials were thoroughly rinsed using UHPW (x5). Vials were then fluxed (lids closed) at 120°C overnight, firstly with concentrated HNO_3 (2 mL, 16 M), then concentrated HCl (2 mL, 12 M), with abundant rinsing with UHPW (x3) between and after fluxes. Vials and lids were finally dried in a ducted laminar flow hood (HEPA-100 class) and double bagged in clean polyethylene bags until use.

2.4 – Sample digestion

The following steps 2.4.1 to 2.4.4 were performed sequentially on each digest batch. The digestion method was a modification of methods employed by Bowie et al. (2010). Vial digests were performed open (un-capped) due to small digest volumes and need for evaporation. Procedural blanks were included in each digest batch and consisted of 2 to 3 empty vials that received the same additions of reagents and isotope spikes to test cleanliness of reagents, spikes, procedures and any cross contamination between vials during digestion.

2.4.1 – Peroxide/nitric acid oxidation

Samples were first oxidised with hydrogen peroxide (H_2O_2) and HNO_3 to partially digest samples in preparation for isotope spike addition (§2.4.2) and avoiding potential spike mass recording errors from addition to dry sediment. To each dry sample, H_2O_2 (1 mL, 9.8 M) and concentrated HNO_3 (1 mL, 16 M) were added and heated without lids at 60°C on a Teflon coated hotplate. After one hour, vials were capped and heat turned off, with vials left to cool overnight.

2.4.2 – Isotope spiking

The technique of isotope dilution (ID) was employed to improve accuracy in determining thorium and uranium concentrations in SOTS sediment samples (Stracke et al., 2014). Briefly, isotope dilution operates on the principle of adding a known quantity of isotope enriched spike to a sample. The relative mass spectrometric signal intensity between isotopes of a target element can then be used to back-calculate the concentration of target isotope, since the chemical behaviour of isotopes is analogous and the dilution factor of isotopes in the sample is known because of the spike (Stracke et al., 2014). Subsequently, spikes of enriched ^{230}Th and ^{236}U in dilute HNO_3 (0.8 M) were used for the determination of ^{232}Th and ^{238}U isotopes, owing to negligible concentrations of ^{230}Th and ^{236}U in sinking marine particles. Samples were spiked with ^{230}Th (50 µL, 49157 pg/g) and ^{236}U spike (250 µL, 48137.1 pg/g), with vials tared prior to each spike addition and the mass of spike recorded. Samples were left to equilibrate for a minimum of 48 hours prior to heating at 150°C until dry.

2.4.3 – Strong acid digestion

To decompose all components of the sample matrix and labilize all trace metals, a combination of strong acids was used. To each dry sample, concentrated HCl (1 mL, 12 M), concentrated HNO_3 (4 mL, 16 M) and HF (300 µL, 29 M) were added before heating vials at 150°C until dry. HNO_3 (4 x 1 mL, 16 M) was then added to each vial with dryness between each addition to remove residual HF, the final addition leading to turning off the heat. Vials were capped and left overnight on the still warm hotplate, importantly enabling the samples to flux for a time.

2.4.4 – Perchloric acid oxidation

Due to the presence of residual organic material in some samples, final oxidation of samples by $HClO_4$ was used to free and labilize remaining complexed trace metals. To each vial, $HClO_4$ (1 mL, 12 M) was added prior to heating at 220°C until dry. To each still hot vial, concentrated HNO_3 (3 x 1 mL, 16 M) was added and continually heated to dryness between each addition to remove traces of $HClO_4$. Finally, heat was turned off and concentrated HNO_3 (2 mL, 16 M) was added to each vial prior to fluxing at 60°C for three days. After cooling, the content of each vial was transferred to a clean, labelled and tared 10 mL PP tube. Each vial was rinsed with UHPW (2 x 1mL) with both rinses added into the 10 mL tube. The mass of the final diluted sample (~4 mL, 8 M HNO_3 solution) was recorded, solution was visually inspected for clarity and sample stored at room temperature prior to analysis.

2.5 – Sample analysis by ICP-MS

Digested samples were analysed by high resolution inductively coupled plasma mass spectrometry (HR-ICP-MS) performed at the Central Science Laboratory (CSL), University of Tasmania. Each analysis session was comprised of a single digest batch of references, blanks and SOTS sediment samples. To assess instrument drift through analysis sessions, an ^{115}In internal calibration standard was used. To a clean, labelled and tared 10 mL plastic tube, 1.000 g of digest (in 8 M HNO_3) was added, followed by 1.000 mL of ^{115}In internal standard (1000 ± 3 µg/mL High Purity Standard (HPS) stock solution). UHPW was added to make up to 10.000 g, resulting in a 1:10 dilution by mass of each digest and ^{115}In internal standard concentration of 100 ng/g. The instrument, Thermo Scientific Element 2 HR-ICP-MS (Thermo Fisher Scientific, Bremen, Germany) was linearly calibrated for each target analyte (Table 1) using LGC VHG Labs MISA standards. While a large suite of elements was analysed, a subset (Al, Ti, V, Fe, Pb, Th) was focussed on for the purposes of this study.

Table 1. List of isotopes analysed by ICP-MS in this study. Acquisition was performed in low and medium resolution modes in order to optimise low mass isotopes detection where polyatomic interference may occur (Bowie et al., 2010). Isotopes in bold indicate tracers of lithogenic material used in this study.

Low resolution					
^{88}Sr	^{107}Ag	^{137}Ba	^{146}Nd	^{187}Re	^{230}Th
^{89}Y	^{109}Ag	^{138}Ba	^{169}Tm	^{205}Tl	**^{232}Th**
^{95}Mo	^{111}Cd	^{139}La	^{171}Yb	^{208}Pb	^{236}U
^{98}Mo	^{133}Cs	^{140}Ce	^{185}Re	^{229}Th	^{238}U
Medium resolution					
^{23}Na	^{31}P	^{45}Sc	^{51}V	**^{56}Fe**	^{63}Cu
^{24}Mg	^{32}S	**^{47}Ti**	^{52}Cr	^{59}Co	^{66}Zn
^{27}Al	^{42}Ca	^{49}Ti	^{55}Mn	^{60}Ni	^{68}Zn

Instrument cleanliness and stability was monitored by in-house quality control (QC) standards prepared by CSL. QC analysis was performed every 10 samples followed by a rinse (UHPW). Analysis of QC samples indicated that instrument drift by linear calibration was significant only for ^{232}Th. Subsequently, ^{232}Th concentration data by linear calibration was not used. Reported concentrations of ^{232}Th and lithogenic flux calculations using ^{232}Th thus come from isotope dilution values and not ICP-MS linear calibration ^{232}Th standard values.

2.5.1 – Rinse analysis

A rinse injection (5% HNO_3) was analysed at the beginning, end and every 10 samples during analysis sessions to a minimum of 7 rinses per session. Across all batches, rinse concentrations did not exceed 1.6 ppb for Al, 0.07 ppb for Ti, 0.70 ppb for Fe, and 0.05 ppb for ^{232}Th. No patterns of accumulation were observed in rinse profiles indicating that sample carryover (for lithogenic tracers) was not apparent.

2.5.2 Repeated sample injections over the course of analytical runs

Further to rinse analysis, a subset of three samples from one analytical session was re-injected at the conclusion of the session to determine if changes in the instrument sensitivity or drift were affecting concentration data. The three re-injected samples provided spacings of 25, 32 and 39 sediment samples between the initial and repeated injections. Average relative standard deviation for the three paired (initial-repeat) sample concentrations were 5.73% for Al, 5.86 % for Ti, 6.44% for Fe, 3.20% for ^{232}Th by isotope dilution. Differences between paired samples were usually an increase in concentration indicating a small degree of instrument calibration drift towards increasing concentrations of Al, Ti and Fe. However, sample accumulation was ruled out as rinses were deemed clean and ^{232}Th by isotope dilution showed good consistency.

2.5.3 – Variability between digest batches using reference materials and samples

Relative standard deviation for key lithogenic tracers between all digest batches of in-house (TT1811-MC45) sediment reference was less than 8% (n = 6; Al = 7.57%, Ti = 3.60%, Fe = 5.44%, ^{232}Th (ID) = 4.51%). Recovery based on previous in house TT1811-MC45 digestion using all analytes (Table A1) produced 105.80 %, while just lithogenic tracers of Al, Ti and Fe (Th by ID not available) indicated recovery of 104.19 %. TT1811 MC45 concentration data is provided in Table A1. Increased concentrations leading to higher recoveries compared to previous in-house digestion may be due to the use of $HClO_4$ in this study leading to improved digestion efficiency (cf. Durand et al. (2017)).

BCR-414 was not certified for any lithogenic tracer concentrations, however average sample recovery based on BCR-414 certified metals (V, Cr, Mn, Ni, Cu, Zn, Pb) was 89.9%. Average recovery based on BCR-414 indicative concentrations of some trace metals (Fe, Co, Sc, Sr, Mo) was 90.50%. Average BCR-414 recovery based solely on Fe was 91.85%. BCR-414 concentration data is provided in Table A2. A dearth in reference materials certified for Al, Ti,

Fe and Th and finding a reference material with a matrix representative of mineral rich sinking sediments (not plankton and not benthic sediment) was identified as an analytical hinderance and requires remedy for future work.

Five SOTS sediment samples were also digested a second time to confirm digest batch repeatability in addition to reference materials. Here, average relative standard deviation across the five paired samples between digest batches 1 and 2 was 4.50% for Al, 5.77% for Ti, 4.43% for Fe, 6.04% for Th (ID), indicating ~5% variation between digest batches. Digest batch replicate concentration data is provided in Table A3.

2.6 – Data processing and analysis

Raw ICP-MS concentrations were blank-subtracted using procedural blanks (§2.4) run during each respective digest batch. The concentration of target elements (Z) in dry samples was calculated from blank subtracted ICP-MS concentrations of each target in the 4mL digest mass ([$digest_{4mL}$]). Dilution factors from the digestion procedure and ICP-MS sample preparation were accounted for in this calculation (Equation 2).

$$[Z_{Sediment}] = [digest_{4mL}] \times 10 \times \left(\frac{digest_{4mL}\ mass}{sediment\ mass}\right) \quad \textbf{(2)}$$

2.6.1 – Lithogenic flux derivation

In order to calculate the flux of lithogenic particles reaching the depth of 1000m, four lithogenic tracers Al, Ti, Fe and ^{232}Th (referred to as Th hereafter) were used. Al, Ti and Th are useful tracers of lithogenic material in the open ocean, being almost exclusively of lithogenic origin and having little if any biological utility (Brewer et al., 1980; Otosaka et al., 2004; Boës et al., 2011; Hsieh et al., 2011; Lam and Marchal, 2015; Ohnemus and Lam, 2015; Anderson et al., 2016; Baker et al., 2016; Kienast et al., 2016; Hayes et al., 2017). Whereas Fe is a vital nutrient for the marine microbiota (Geider and Laroche, 1994), the abundance of this metal in sinking marine sediments at depth may also stem from the transport of biological organisms and iron-binding ligands by ocean currents in addition to lithogenic inputs (Hunter and Boyd, 2007; Boyd and Ellwood, 2010; Gledhill and Buck, 2012). The use of multiple tracers enables assessment of the variability in lithogenic material between different tracer techniques, improving determination of the fraction sinking particle flux as lithogenic material (Ohnemus and Lam, 2015).

Elemental fluxes (F_Z) in mg m^{-2} d^{-1} were estimated for each lithogenic tracer by multiplying the Al, Ti, Fe and Th concentrations measured in sediment trap samples by the total mass flux (TMF) of the respective cup (Equation 3).

$$F_Z=[Z_{Sediment}]\times TMF \quad \textbf{(3)}$$

Total lithogenic particle fluxes ($F_{Lith,\ Z}$) were calculated using each of the selected tracers by dividing the elemental flux of respective tracers (F_Z) by their globally averaged upper continental crust (UCC) concentrations ($[Z]_{UCC}$; Equation 4). Tracer globally averaged UCC concentrations were obtained from Rudnick and Gao (2003).

$$F_{Lith,\ Z}=\frac{F_Z}{[Z]_{UCC}} \quad \text{(Z = lithogenic tracer; } ^{27}\text{Al, } ^{47}\text{Ti, } ^{56}\text{Fe or } ^{232}\text{Th)} \quad \textbf{(4)}$$

2.6.2 – Lithogenic flux from mass balance

A recent assessment of sinking sediment biogenic component fluxes at SOTS over the past two decades by Wynn-Edwards et al. (2020) indicated lithogenic particle fluxes at SOTS 1000m may account for up to 10% of TMF. This estimation was based off the mass balance of the total mass flux as the sum of major biogenic component fluxes (F_{PIC}, F_{BSi}, F_{POM}) and lithogenic component ($F_{Lith,\ MB}$) to a theoretical TMF of 100% (Equation 5). Comparison of lithogenic particle fluxes by mass balance to lithogenic particle fluxes by chemical tracers is examined to quantify differences between the methods.

$$TMF = F_{PIC} + F_{BSi} + F_{POM} + F_{Lith,\ MB} \quad \textbf{(5)}$$

Where F is a fraction of TMF, also called total biogeochemical mass balance (mass balance).

The calculation of $F_{Lith,\ MB}$ by mass balance is thus made under the assumption that the remaining fraction of the TMF minus biogenic flux components can be attributed to lithogenic material as shown in Equation 6. This method has been used by a number of sediment trap studies to estimate lithogenic particle fluxes (Wefer and Fischer, 1993; Ratmeyer et al., 1999b; Francois et al., 2002; Helmke et al., 2005; Fischer et al., 2009; Nowald et al., 2015; Wynn-Edwards et al., 2020; Harms et al., 2021).

$$F_{\text{Lith, MB}} = \text{TMF} - F_{\text{PIC}} - F_{\text{BSi}} - F_{\text{organic matter}} \equiv \text{TMF} - F_{\text{CaCO}_3} - F_{\text{BSiO}_2} - 2.2 \times F_{\text{POC}} \quad \textbf{(6)}$$

Where:

POM (particulate organic matter) = 2.2×POC from Klaas and Archer (2002).

F = TMF component flux

PIC (inorganic carbon) and BSi (opal) fluxes being estimated from their most abundant molecular forms, $CaCO_3$ and $BSiO_2$ respectively (Wynn-Edwards et al., 2020).

2.6.3 – Other calculations

Enrichment factors were calculated to study the enrichment of each lithogenic tracer relative to the other tracers used, as well tracers of anthropogenic emissions. This analysis provides information on the enrichment of a suite of elements (Al, Fe, Pb, Th, Ti, V) relative to 3 of our lithogenic tracers (Al, Th and Ti, Fe being subjected to further variability). The aim of calculating such enrichment factors in SOTS sediment samples is to enable comparison with reported enrichment in aerosols and alluvial dusts from different potential source regions in Australia. Enrichment factor for an element (Z) was calculated as the concentration ratio of Z relative to each lithogenic tracer (Al, Ti, Th) using Equation 7 compared to reported global UCC concentration ratios (Rudnick and Gao, 2003).

$$\text{EF}_Z = \frac{[Z]_{\text{sample}}/[\text{tracer}]_{\text{sample}}}{[Z]_{\text{UCC}}/[\text{tracer}]_{\text{UCC}}} \quad \textbf{(7)}$$

Pearson's correlation coefficient (*r*) was used to quantify linear relationships between particle flux components and also lithogenic tracer concentrations in samples. Determination of significance in observed correlations was established by the Pearson critical value of $p = 0.05$ for significant correlation.

2.7 – Remote sensing observations

To examine the factors that might contribute to lithogenic particle flux patterns at SOTS, such as dust deposition, as well as direct productivity responses, a range of remotely sensed observations and a satellite re-analysis product were examined.

Aerosol optical depth (AOD) from MODIS-Aqua remotely sensed reflectance at 869 nm was used to generate a time series of aerosol loading above SOTS over the study time period. 8-day AOD area-averaged for a 2°x2° box around SOTS (47.98°S 141.02°E, 46.02°S 142.98°E) was provisioned from Giovanni (Acker and Leptoukh, 2007; NASA Goddard Space Flight Center, 2018b).

To investigate possible productivity responses to increased lithogenic particle delivery at SOTS, 8-day ocean surface chlorophyll a concentration area-averaged for a 2°x2° box around SOTS (47.98°S 141.02°E, 46.02°S 142.98°E) over the study period was obtained from MODIS-Aqua satellite data provisioned from Giovanni (Acker and Leptoukh, 2007; NASA Goddard Space Flight Center, 2018a).

In addition to AOD, the Modern-Era Retrospective analysis for Research and Applications, Version 2 (MERRA-2) satellite re-analysis model for dust deposition (GMAO, 2015) was examined over SOTS across the study period. Since MERRA-2 incorporates satellite measurements of AOD, MERRA-2 modelled dust deposition provides a plausible link between atmospheric aerosol loading and deposition to the ocean surface. MERRA-2 modelled dust deposition was provisioned from Giovanni (Acker and Leptoukh, 2007; NASA Goddard Space Flight Center, 2018b) using mean monthly area averaged total wet and dry deposition for the region 48.00°S 141.88°E, 46.00°S 143.13°E.

3. Results

3.1 - Lithogenic particle flux estimates at SOTS, 1000m depth, 2010-2019

Obtained lithogenic particle flux estimates using each lithogenic tracer were compiled for the 124 samples to generate a time-series of lithogenic flux at SOTS at 1000m depth (Figure 3). The variability of F_{Lith} estimates across the four tracers demonstrated good agreement, with magnitude only varying up to a factor of 2. Lithogenic particle flux estimate based on Fe measurements produced the highest F_{Lith} and Th-based estimates defined F_{Lith} lower bound.

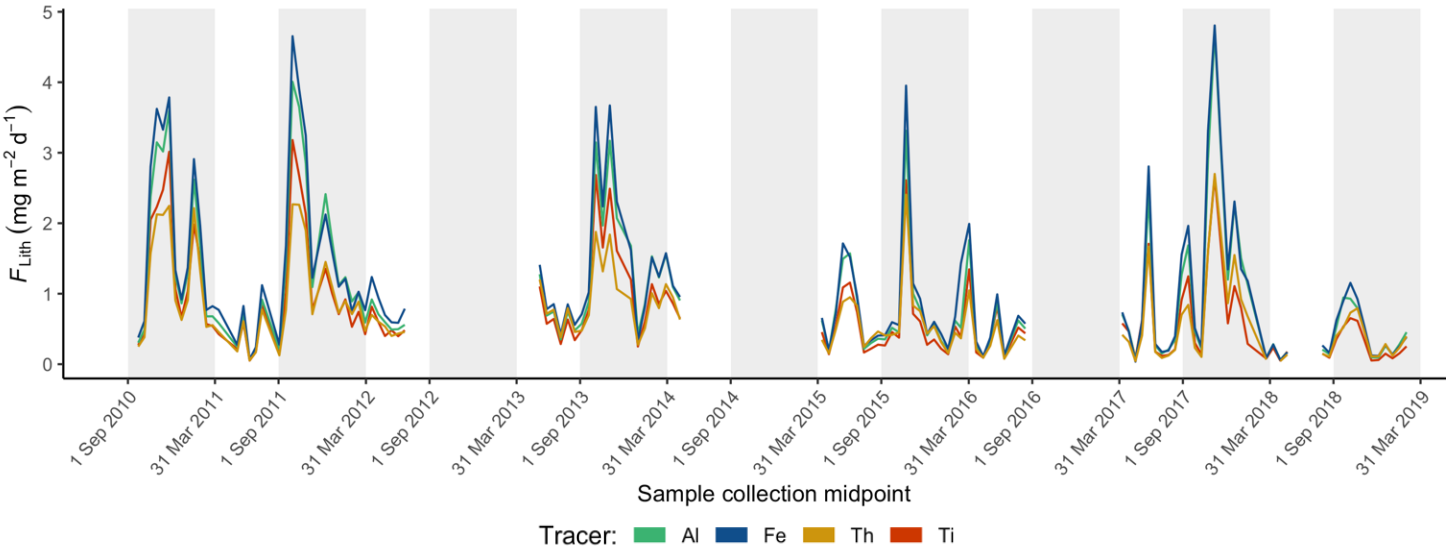

Figure 3. Lithogenic particle flux (F_{Lith}) estimates at 1000m depth derived from measurements of Al (green), Fe (blue), Th (yellow), and Ti (red) in sediment trap samples collected at SOTS between 2010 and 2019. Sample collection midpoint is the date corresponding to half of the sampling period for each sediment collection. Gaps in the time series result from insufficient material in sediment trap samples to overcome analytical detection limits or from a lack of trap deployment (see §2. Methods).

Lithogenic flux estimates from the four tracers (Figure 3) were averaged to produce a multi-tracer mean lithogenic flux (F_{LithAv}) in order to reduce bias from choosing one tracer and better estimate lithogenic particle flux variability (Figure 4a). Peaks in F_{LithAv}, over 3 mg m^{-2} d^{-1} (Figure 4a), were observed during the Austral spring-summer season from September to March. This peak flux period coincides with previous observations at SOTS of TMF and biogeochemical component fluxes by Trull et al. (2001) and Wynn-Edwards et al. (2020). Monthly averages were calculated across all years with relatively consistent sampling coverage

(Figure 4b). F_{LithAv} seasonal variability was characterised by a main peak in November (spring/early summer), with a second, more variable, flux peak of smaller magnitude in February (late summer) (Figure 3, Figure 4a, b). Conversely, the lowest mean monthly F_{LithAv} was observed in July (winter, Figure 4b), however noticeable increases in F_{LithAv} occurred during the winters 2015 and 2017 (Figure 3, Figure 4a).

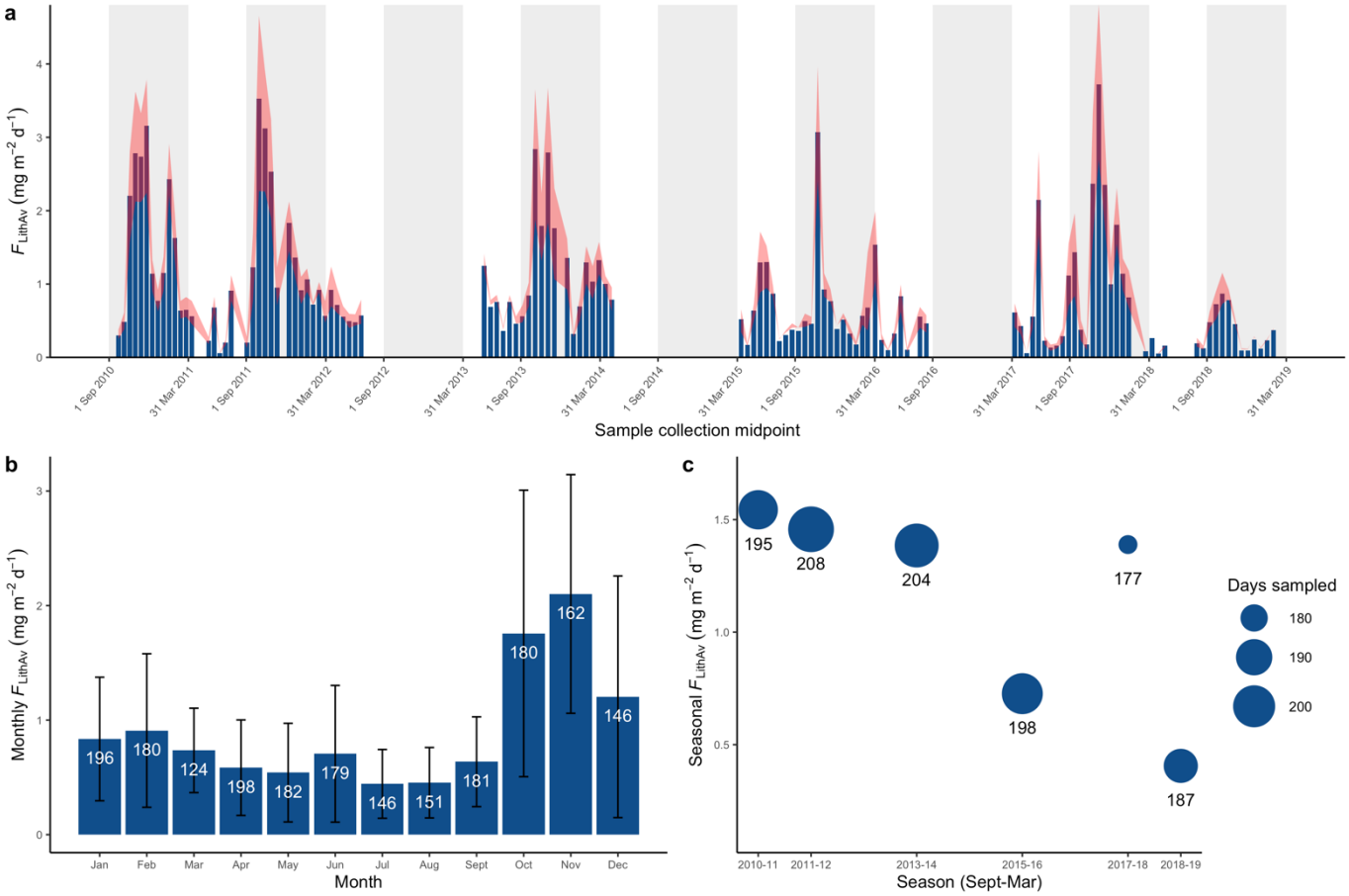

Figure 4. a) Lithogenic particle flux estimate (F_{LithAv}) averaged from all lithogenic tracers (Al, Ti, Fe and Th, Figure 3). Blue bars denote sediment trap cup samples analysed in this study, red shading denotes upper and lower bounds of individual tracer estimates shown in Figure 3. Grey shading indicates the spring-summer season from September to March. **b**) Mean monthly F_{LithAv} calculated across all years. Error bars denote 1 standard deviation from the mean and white numbers denote the total number of days sampled in each month across all years. **c**) Mean F_{LithAv} during the austral spring-summer excluding 2012-13, 2014-15 and 2016-17 seasons due to a lack of data (see methods section). Total days sampled throughout each season is given (maximum 211 days possible).

Seasonal averages were calculated for the spring-summer period (September-March) of each year presenting consistent sampling coverage (Figure 4c). Highest mean seasonal F_{LithAv}

values, around 1.5 mg m^{-2} d^{-1}, were observed during spring-summer seasons of 2010-11, 2011-12, 2013-14 and 2017-18, while much lower fluxes of 0.4-0.7 mg m^{-2} d^{-1} were recorded in 2015-16 and 2018-19 seasons (Figure 4c). The lowest mean summer F_{LithAv} of 0.5 mg m^{-2} d^{-1} occurred in 2018-19 (Figure 4c). The absence of data for seasons 2012-13, 2014-15 and 2016-17 prevented determination of any decadal trend in mean seasonal F_{LithAv}. Despite gaps in data collection and inconsistent sampling between years, sampling coverage over the entire analysis period was relatively consistent between months (Figure 4b). The average F_{LithAv} across all samples (i.e. average of all months presented in Figure 4b) was 0.91±0.87 mg m^{-2} d^{-1} (Table 2).

3.2– Comparison to previous subantarctic lithogenic particle flux estimates

Lithogenic particle flux estimates to the Australian-New Zealand (NZ) sector of the subantarctic (SAZ) Southern Ocean were compiled from previous studies, incorporating various measurement techniques and model estimates of dust deposition to the study area (Table 2). Additionally, a recent timeseries compilation of export fluxes at SOTS (Wynn-Edwards et al., 2020), using the same samples as those analyzed in this study, was used to estimate lithogenic particle flux by mass balance calculation described by equations 5 and 6 (§Methods 2.6.2). Thus, a maximum possible lithogenic flux ($F_{Lith, MB}$) was estimated using the mass balance equation (Equation 6) from Wynn-Edwards et al. (2020).

Comparison of the F_{LithAv} estimate to lithogenic flux by mass balance calculation, $F_{Lith, MB}$ (calculated using data reported in Wynn-Edwards et al., 2020), resulted in $F_{Lith, MB}$ on average 6.7 times greater than F_{LithAv} (Figure 5, Table 2). While lithogenic flux at 1000m depth was proposed to contribute as much as 10% of TMF at SOTS (Wynn-Edwards et al. 2020), our F_{LithAv} estimate at this site and depth is far lower, representing about 1-2% of TMF (Table 2), in line with previous estimates using Al-tracer technique (Trull et al. 2001; Table 2). Greater difference in lithogenic flux magnitude between F_{LithAv} and $F_{Lith, MB}$ was observed during the spring summer season (Figure 5b). In the spring-summer season, $F_{Lith, MB}$ secondary seasonal peaks in late summer occurred at greater relative magnitude than initial spring peaks compared to F_{LithAv} peak flux patterns (Figure 5b). This may be indicative of additional components of the TMF contributing to the TMF residual mass balance that have not been accounted for so far. The higher correlation between $F_{Lith, MB}$ with biogenic TMF components of POC and opal,

compared to F_{LithAv} correlation with POC and opal (Table 3) might indicate additional biogenic mass flux components not previously analysed at SOTS (see §3.3).

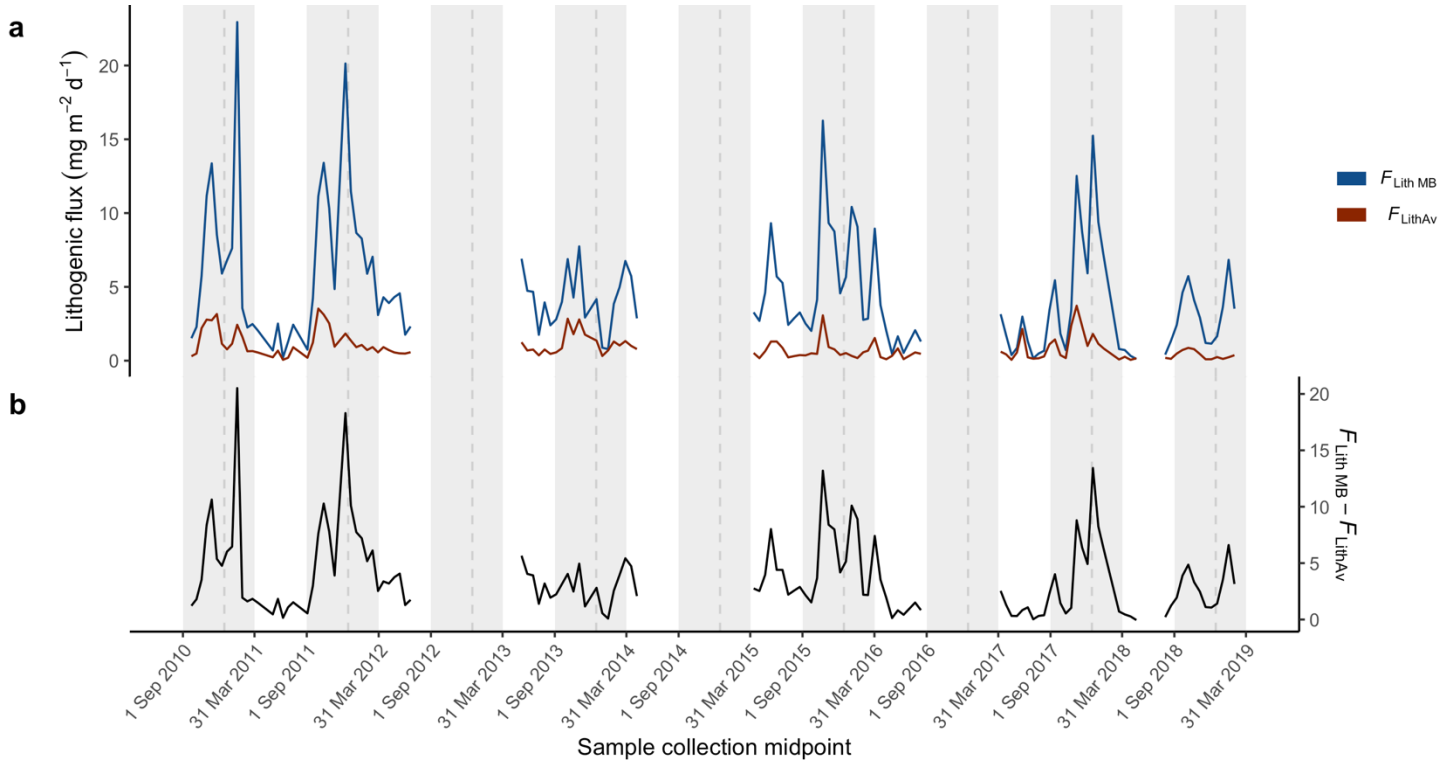

Figure 5. a) Comparison of this studies multi-tracer averaged lithogenic particle flux (F_{LithAv}, red line) with mass balance-derived maximum lithogenic flux, $F_{Lith,\ MB}$ (blue line). Calculation of $F_{Lith,\ MB}$ was derived from the TMF mass balance equation (6) and data reported in Wynn-Edwards et al. (2020). b) Difference in lithogenic flux (mg m^{-2} d^{-1}) between $F_{Lith,\ MB}$ and F_{LithAv}. Dashed line denotes 1st of January in each sampling year.

Earlier 1000m-deep lithogenic particle flux estimates calculated at SOTS (based on Al tracer, Trull et al., 2001) range between 1.04 and 1.31 mg m^{-2} d^{-1}, falling within the higher range of F_{LithAv} estimated in this study (0.91±0.83 mg m^{-2} d^{-1}, Table 2), which corresponds to our Fe tracer-based F_{Lith} estimate ($F_{Lith,\ Fe}$ = 1.14±1.07; Figure 3, Figure 4a). Similarly, Al-tracer flux estimate at 1500m depth in subantarctic waters south-east of NZ by Nodder et al. (2016) of 1.2±1.5 mg m^{-2} d^{-1} is comparable to F_{LithAv} of ~1.5 mg m^{-2} d^{-1} in higher seasons (Figure 4c). Nodder et al. (2016) note that 1500m deep lithogenic particle flux (Nodder et al. 2016 Figure 9) does not display marked seasonality in their study region, contrasting with the strong seasonality observed in our F_{LithAv} at 1000m at SOTS (Figure 4a, b). Additionally, the proportion of TMF associated with lithogenic material is higher in Nodder et al.'s estimate (3.9±5.9 %) compared to SOTS (1.7±0.8 %). Differences between lithogenic fluxes at SOTS and southeast of NZ (Nodder et al., 2016) are possibly due to the different oceanographic

setting (productivity and downstream proximity to continental shelf and fluvial lithogenic sources).

Table 2. Estimates of the mean lithogenic particle flux and dust deposition to surface water (in mg m^{-2} d^{-1}) from field studies and model outputs, respectively, in the Australian-NZ sector of the subantarctic Southern Ocean. The proportion (%) of the total mass (TMF) flux associated with lithogenic flux estimate is also reported where available. Where possible, data is only reported for the SOTS study area (2°x2° box around 47°S, 142°E) specifically.

Data source	**Mean lithogenic flux**	**Method**	**Location & depth**	**Period**
This study, F_{LithAv}	0.91±0.87 1.68±0.77 % of TMF	Sinking particles [Al, Ti, Fe, ^{232}Th]	SOTS, 1000m	2010-2019
Nodder et al. (2016)	1.20±1.50 3.90±5.90 % of TMF	Sinking particles [Al], 8.4 % UCC	46°40'S 178°30'E 1500m	2001-2011
Wynn-Edwards et al. (2020)	4.66±4.08* 8.64±3.64* % of TMF	Sinking particles TMF mass balance	SOTS, 1000m	2010-2019
Trull et al. (2001)	1.04 – 1.31	Sinking particles [Al], 8.4 UCC %	SOTS, 1000m	Sept 1997- Feb 1998
Weis et al., Unpublished	1.68±0.08	^{230}Th normalised flux from benthic sediment	SOTS, 4474m	Last ~500 years
Bowie et al., (2009)	0.37±0.18	Aerosol [Al], 7.7% UCC	SOTS, surface	Summer 2007
	Mean dust deposition	**Model**	**Region**	**Simulation period**
Albani et al. (2014)	0.55 – 5.48	CAM4 DustDep	SAZ below TAS	2020 - 2030
Mahowald et al. (2006)	1.37 – 5.48	CCSM3 (CAM3) DustDep	SAZ below TAS	1996 - 2006
NASA (2018b)	1.88±0.91	MERRA-2, monthly mean	SOTS area	2010 - 2019

***** Calculated from data published in Wynn-Edwards et al., 2020. Data available at portal.aodn.org.au

Alternatives methods for lithogenic flux estimation at SOTS were also examined (Table 2). Lithogenic flux calculated at SOTS from aerosol samples during the SAZ-Sense cruise (21 January to 19 February 2007) produced a smaller estimate of 0.37±0.18 mg m^{-2} d^{-1}. An estimate from ^{230}Th-normalised lithogenic flux (Francois et al., 2004; Anderson et al., 2016) from a core-top sediment sample from SOTS by Weis et al. (unpublished) of 1.68±0.08 mg m^{-2} d^{-1} agrees with seasonal F_{LithAv} averages of 1.5 mg m^{-2} d^{-1} (Figure 4c), but pushes the upper limit of the overall F_{LithAv} (0.91±0.83 mg m^{-2} d^{-1}).

Lithogenic particle flux estimates were also compared to models of dust deposition to both validate models and aid investigation into lithogenic particle source attribution. As shown in Table 2, Community Atmosphere Model (CAM; versions 3 and 4) estimates of dust deposition (Mahowald et al., 2006; Albani et al., 2014) to the surface subantarctic ocean south of Australia (range 0.55 – 5.48 mg m^{-2} d^{-1}) capture the range of 1000m lithogenic particle flux variability (0.05 mg m^{-2} d^{-1} < F_{LithAv} < 3.72 mg m^{-2} d^{-1}) observed at SOTS, but may overestimate dust contributions to lithogenic particle flux. MERRA-2 estimate (2°x2° area averaged) of mean wet and dry dust deposition over SOTS (1.88±0.91 mg m^{-2} d^{-1}) is twice greater than F_{LithAv}, (0.91±0.83 mg m^{-2} d^{-1}). Equivalency of dust deposition and lithogenic particle fluxes is discussed in §4.3.4)

3.3– Correlation between components of the TMF

To examine a potential link between 1000m lithogenic particle flux and export production at SOTS, TMF and major biogeochemical flux components such as $CaCO_3$, $BSiO_2$ and POC (Wynn-Edwards et al., 2020) were compared to our estimates of F_{LithAv} (Figure 6, Table 3). F_{LithAv} showed a slightly different seasonal pattern compared with major biogeochemical components. Seasonal F_{LithAv} peaked in late spring-summer, with a secondary seasonal spike of reduced magnitude occurring in late summer (Figure 4b; Figure 6h). Conversely, secondary peaks in TMF and $CaCO_3$, $BSiO_2$ and POC fluxes were characterised by similar or higher magnitude than the initial spring-summer peak for the 2010-11, 2011-12 and 2017-18 seasons (Figure 6a, b, c, d). This same pattern was also observed for $F_{Lith, MB}$ estimates (Figure 5). Indeed, correlation between $F_{Lith, MB}$ and TMF (0.881, $p < 0.001$) was higher than that between F_{LithAv} and TMF (0.841, $p < 0.001$; Table 3), but both correlations were strong and significant (Pearson's correlation test). Similarly, $F_{Lith, MB}$ correlation with both POC and $BSiO_2$ (0.802 and 0.774 respectively, $p < 0.001$) was higher than correlation of F_{LithAv} with POC and $BSiO_2$ (0.682 and 0.656 respectively, $p < 0.001$). These observations indicate the use $F_{Lith, MB}$ may lead to misinterpretation of the role of lithogenic material in both productivity connections and mineral ballast of POC (see §4.6).

Table 3. TMF and flux component correlation matrix using Pearson's correlation value (*r*). All correlations were significant at $p < 0.001$ across all correlations (n = 124).

	TMF	$CaCO_3$	POC	$BSiO_2$	LithAv	Lith, MB
TMF	-	-	-	-	-	-
$CaCO_3$	0.975	-	-	-	-	-
POC	0.901	0.805	-	-	-	-
$BSiO_2$	0.816	0.712	0.822	-	-	-
LithAv	0.841	0.856	0.682	0.656	-	-
Lith, MB	0.881	0.810	0.802	0.774	0.707	-

Significant F_{LithAv} variability compared to TMF component fluxes was observed between seasons and a consistent pattern was hard to define. While seasonal F_{LithAv} peaks of nearly 3 mg m^{-2} d^{-1} occurred in the 2013-14 season, TMF, $CaCO_3$, $BSiO_2$ and POC fluxes remained low (Figure 6). The 2018-19 season demonstrated low F_{LithAv} and low fluxes in all TMF components compared to previous years (Figure 6). Despite this variability, F_{LithAv} correlation to TMF component fluxes across all years was highest with $CaCO_3$ flux, showing a strong and significant correlation ($r = 0.856$, $p < 0.001$; Table 3). This was not surprising since previous studies show $CaCO_3$ is the predominant component (> 60%) of the TMF at 1000m depth (Wynn-Edwards et al., 2020) due to the prevalence of coccolithophores at SOTS (Rigual Hernández et al., 2018; Rigual Hernández et al., 2020).

3.4 – Lithogenic particle composition

The composition of lithogenic particles was compared to global averaged UCC elemental ratios (Rudnick and Gao, 2003) in order to identify potential elemental enrichment (Equation 7) in 1000m-deep sediments at SOTS. Comparisons were made between enrichment factors in our 1000m sediment samples at SOTS and enrichments factors of SOTS benthic sediments (KC07 0cm core), BCR-414 (plankton sediment), and mineral dusts from known Australian dust source regions previously reported in the literature (Kamber et al., 2005; Marx et al., 2005b, 2005a; McGowan et al., 2005). Enrichment factor data is summarised in Table 4. Australian sources were investigated as atmospheric transport models (e.g. HYSPLIT) suggest that the south-eastward transport of dust particles from central Australian arid areas may represent the prevalent air-mass to the Southern Ocean south of Australia, including SOTS (Bowie et al., 2009; O'Loingsigh et al., 2017). Enrichment factors for all sediment samples collected at SOTS demonstrated a good alignment with UCC ratios relative to the different lithogenic tracers (<2, Table 4). Fe and Al were slightly enriched compared to Ti and Th tracers, but Fe/Al ratios were

close to global UCC, as were Ti/Th ratios. Detailed comparisons to enrichment factors are made in §4.3.

While slight iron enrichment in 1000m sediment samples may be due to atmospheric input of aerosols that are enriched in iron, in the ocean biological utilisation of Fe (Twining and Baines, 2013) can also impact Fe enrichment observed in sediment samples (Rauschenberg and Twining, 2015). To test this, Fe enrichment factor was examined in the certified plankton reference material BCR-414 and compared to SOTS 1000m sediments (Table 4). Concurrently, Fe concentrations were correlated against lithogenic tracer concentrations in SOTS 1000m sediments (Table 5) to test Fe concentrations association strength to more conservative lithogenic tracers Al, Ti and Th. This correlation was also used to assess the use of Al, Ti, Fe and Th tracers as crustal material markers (Figure 3) in SOTS sediments (Table 5).

Fe enrichment relative to Th, Ti and Al was higher in BCR-414 (1.876, 2.321 and 1.512) compared to that in SOTS samples (1.523, 1.528 and 1.117), indicating SOTS samples were not enriched in Fe relative to planktonic concentrations. Very strong and significant correlations (Pearson's correlation test) between concentrations of Fe and Al (0.913, $p < 0.001$), Al and Ti (0.952, $p < 0.001$) and Ti and Th (0.903, $p < 0.001$) were observed in our samples (Table 5). The lowest correlation was observed for lithogenic tracers Fe and Th (0.846, $p < 0.001$). These close to linear and significant correlations, alongside low Fe enrichment compared to BCR-414, strongly indicate that the tracers examined in this study were of lithogenic origin and that Fe in sediment was unlikely to be impacted by biological Fe enrichment (§4.3.1)

Figure 6. a) TMF components at 1000m depth at SOTS 2010-2019 (mg m^{-2} d^{-1}) including b) $CaCO_3$, c) POC and d) $BSiO_2$ fluxes (mg m^{-2} d^{-1}). *Biogeochemical flux data are taken from Wynn-Edwards et al. (2020). e) 8-day surface chlorophyll-a concentration (mg m^{-3}) area averaged over SOTS (47.98°S 141.02°E, 46.02°S 142.98°E) and f) 8-day aerosol optical depth (AOD) area-averaged over SOTS from MODIS-Aqua, NASA. Gaps in data is due to cloud coverage for Southern Ocean winter. g) MERRA-2 satellite reanalysis product of combined wet and dry dust deposition (mg m^{-2} d^{-1}) over SOTS area (48.00°S 141.88°E, 46.00°S 143.13°E. h) multi-tracer average 1000m lithogenic particle flux estimate F_{LithAv} (mg m^{-2} d^{-1}) at SOTS between 2010 and 2019 (as in Figure 4a).

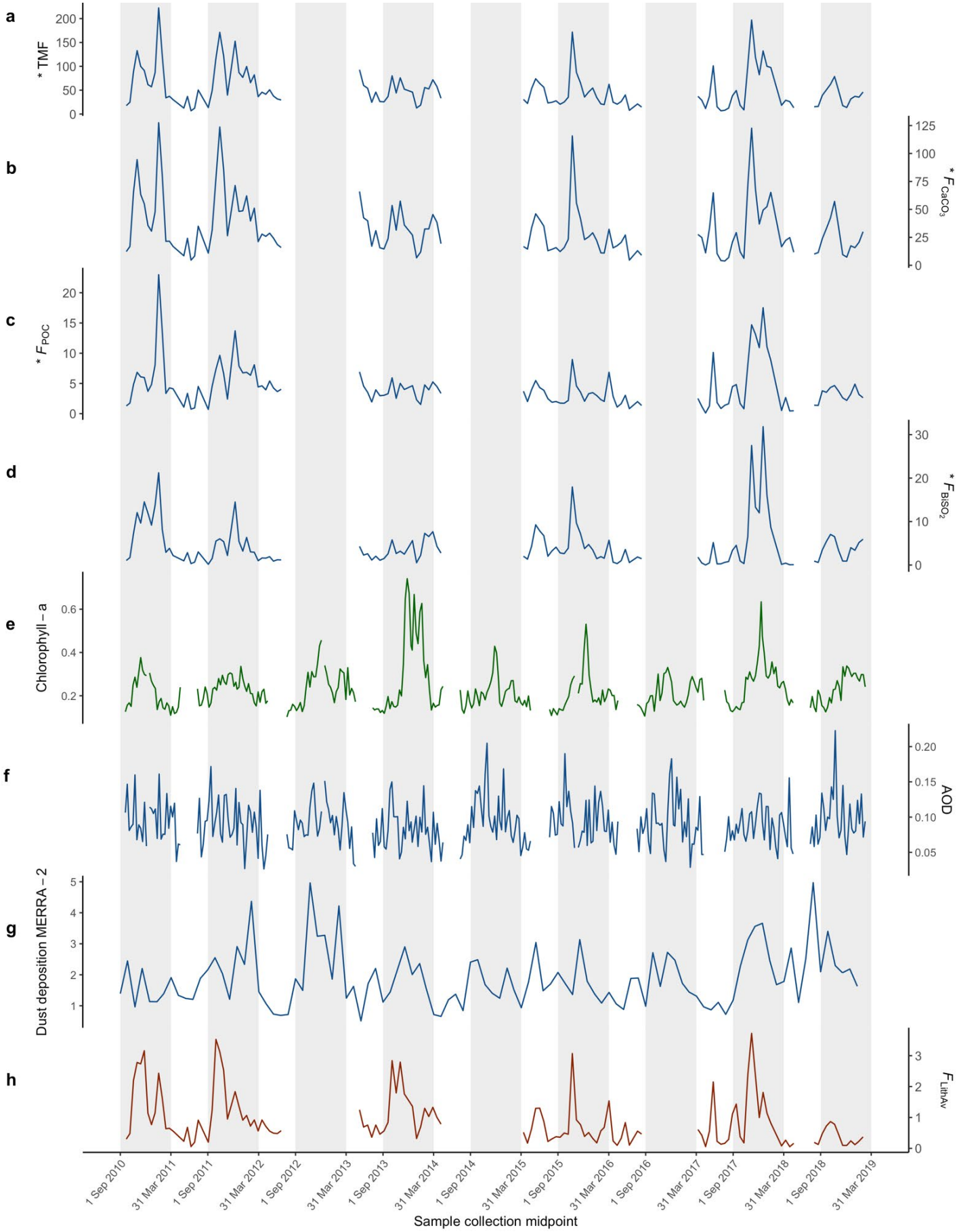
a
* TMF
200
150
100
50
0
b
125
100
75
50
25
0
* F_{CaCO_3}
c
* F_{POC}
20
15
10
5
0
d
30
20
10
0
* F_{BiSO_2}
e
Chlorophyll – a
0.6
0.4
0.2
f
0.20
0.15
0.10
0.05
AOD
g
Dust deposition MERRA – 2
5
4
3
2
1
h
3
2
1
0
F_{LithAv}
1 Sep 2010
31 Mar 2011
1 Sep 2011
31 Mar 2012
1 Sep 2012
31 Mar 2013
1 Sep 2013
31 Mar 2014
1 Sep 2014
31 Mar 2015
1 Sep 2015
31 Mar 2016
1 Sep 2016
31 Mar 2017
1 Sep 2017
31 Mar 2018
1 Sep 2018
31 Mar 2019
Sample collection midpoint

Table 4. Enrichment factors (EF) relative to lithogenic tracers from this study (1000m samples and KC07 bottom surface sediment). For comparison, enrichment factors from a range of alluvial mineral sources from dust emission areas of south-eastern Australia and aerosols representative of southern Australia marine regions are included. Uncertainty (where available) is given as one standard deviation from the mean.

	SOTS 1000m sediments 2010-2019	IN2018_V02 _KC07 0cm Core, SOTS ocean floor	BCR-414 plankton sediment reference	Lake Eyre South, SA	Ceduna, SA	QLD mineral dust (30 sample average)	Darling River, NSW	Cleve, SA	Buronga/ Mildura, NSW-VIC	Southwest marine region aerosol	Southeast marine region aerosol
	This study	This study	This study	*Marx et al. (2005b)*	*Marx et al. (2005b)*	*Kamber et al. (2005)*	*Marx et al. (2005a)*	*McGowan et al. (2005)*	*Marx et al. (2005a)*	*Perron et al., (2020)*	*Perron et al., (2020)*
Location	47° S 142° E	47° S 142° E	Po river, Italy	~29° 30' S ~137° 30' E	32° 07' S 133° 40' E	Queensland < 29° S	30° 41' S 144° 50' E	33° 42' S 136° 29' E	34° 10' S 142° 11' E	112 - 139° E	26 – 38° S
$EF_{Fe/Al}$	1.12±0.19	1.11±0.01	1.51±0.03			1.23				1.2±1.2	1.5±1.2
$EF_{Fe/Ti}$	1.53±0.40	1.27±0.06	2.32±0.01			0.71					
$EF_{Fe/Th}$	1.52±0.39	1.74±0.06	1.88±0.06			1.17					
$EF_{Al/Ti}$	1.38±0.33	1.14±0.06	1.54±0.04			0.58					
$EF_{Al/Th}$	1.37±0.29	1.56±0.07	1.24±0.04			0.95					
$EF_{Ti/Th}$	1.03±0.26	1.37±0.05	0.81±0.03	1.10	1.16	1.65	1.41	0.95	0.88		
$EF_{V/Al}$	2.52±0.92	1.38±0.02	3.04±0.02			1.08				13.4±7.7	50.0±41.8
$EF_{V/Ti}$	3.52±1.73	1.57±0.08	4.67±0.13	0.75	0.43	0.62					
$EF_{V/Th}$	3.35±1.12	2.15±0.09	3.78±0.11	0.83	0.50	1.03					
$EF_{Pb/Al}$	9.14±4.76	1.56±0.03	7.50±0.22			0.94				14.4±6.1	63.2±74.6
$EF_{Pb/Ti}$	12.42±6.74	1.77±0.08	11.51±0.20	0.67	0.72	0.54					
$EF_{Pb/Th}$	11.86±5.08	2.44±0.08	9.30±0.17	0.74	0.84	0.89					

Table 5. Pearson's correlation value (*r*) matrix for lithogenic and anthropogenic tracer concentrations in SOTS 1000m samples. All correlations highly significant at $p < 0.001$ (n = 124 for Fe, Al, Ti, Th and V; n = 123 for Pb, see text).

	Fe	Al	Ti	Th
Fe	1	-	-	-
Al	0.913	1	-	-
Ti	0.894	0.952	1	-
Th	0.846	0.898	0.903	1
V	0.681	0.710	0.649	0.663
Pb	0.529	0.500	0.528	0.608

Concentrations of tracers of anthropogenic emissions, namely V and Pb (Pacyna and Pacyna, 2001; Taylor, 2015; Shelley et al., 2017b; Streibel et al., 2017), were also correlated to lithogenic tracer concentrations in our sediment samples (Table 5) in order to discriminate whether 1000m deep particles at SOTS originate from crustal material or anthropogenic sources. One instance of very high Pb enrichment (EF_{Pb}) exceeding 300 relative to Ti, Al and Th was observed and this outlier removed prior to correlation and enrichment factor calculation. Enrichment in Pb (9.5 – 12.4; Table 4) and very slight enrichment in V (2.5 – 3.5; Table 4) were observed in SOTS sediments. EF_{Pb} in 1000m sediments (EF_{Pb} = 9.1 – 12.4) was considered to be significant due to anthropogenic activities according to Shelley et al. (2017b) criteria of EF_{Pb} >10 indicating enrichment external to natural crustal variability. As such, while EF_V may be slightly high compared to benthic sediments at SOTS (Table 4), it may be due to natural variability in source lithogenic material (Shelley et al., 2017b). Correlation of Pb concentrations to Fe, Al, Ti and Th lithogenic tracer concentrations (0.500 – 0.608, Table 5) was less than lithogenic tracer intercorrelation (0.846 – 0.952, Table 5) but still significant (Pearson's correlation test, $p<0.001$, n = 123).

3.5– Lithogenic flux estimate compared to remotely sensed aerosol optical depth, surface chlorophyll and MERRA-2 modelled dust deposition

To further investigate potential sources of lithogenic particles arriving at SOTS 1000m depth and possible links between dust deposition and productivity, remotely sensed chlorophyll a (Chl a) and AOD data from MODIS-Aqua |(NASA, 2018) over the SOTS study area was examined and compared to MERRA-2 dust deposition reanalysis product from of satellite-based observations (GMAO, 2015). Area-averaged Chl a over SOTS demonstrated spring-summer seasonal maxima (Figure 6e), with mean monthly Chl a between 2010 and 2019 being

the highest in December (Figure 7e). Interestingly, a strong sustained peak in Chl a coincided with our observed F_{LithAv} positive anomaly during the 2013-14 season (Figure 6e), contrasting with low flux of CaCO3 and POC recorded during this season (Figure 6a, b, c, d). Area-averaged aerosol optical depth (AOD) was more variable (Figure 6f), yet the mean monthly trend across 2010-2019 shows a noticeable increase in AOD in September and October and again in January (Figure 7f). MERRA-2 total dust deposition at SOTS showed some similarities with AOD and F_{LithAv} variability at 1000m depth (Figure 6g, h, Table 2). Similar peak periods over spring-summer for AOD (Figure 7f) and MERRA-2 dust deposition (Figure 7g) are not surprising considering the parameterisation of MERRA-2 model using AOD (GMAO, 2015). Notably however, mean monthly MERRA-2 dust deposition was highest from October to January (Figure 7g), coinciding with highest mean monthly F_{LithAv} (Figure 7h).

Lowest TMF, Chl a, AOD and MERRA-2 dust deposition all occurred in winter (Figure 7). All parameters shared the same peak season between September and March, with a progressive shift from the AOD peak to dust deposition peak, then 1000m-deep lithogenic flux maxima. AOD was greatest in September-October, reflecting the largest annual aerosol loading in the atmosphere (Figure 7f). MERRA-2 modelled dust deposition (which is parametrised using AOD) was then highest from October to December (Figure 7g). This deposition trend was followed by the observed peak of 1000m lithogenic particle flux (F_{LithAv}) in November (Figure 7h) and the maximum surface Chlorophyll-a concentration in December (Figure 7e). While both the $CaCO_3$ and F_{LithAv} flux peaks occurred in November (Figure 7b, h), the POC and $BSiO_2$ fluxes only peaked later, in February and December respectively (Figure 7c, d).

Figure 7. Mean monthly a) total mass flux (mg m^{-2} d^{-1}), b) $CaCO_3$ flux (mg m^{-2} d^{-1}), c) POC flux (mg m^{-2} d^{-1}) and d) $BSiO_2$ flux (mg m^{-2} d^{-1}) at SOTS 1000m. Biogeochemical fluxes a-d from Wynn-Edwards et al. (2020). e) Mean monthly surface chlorophyll (mg m^{-3}) from MODIS-Aqua 8-day area averaged for the region 47.98°S 141.02°E, 46.02°S 142.98°E, from 2010-2019. f) Mean monthly AOD (RRS at 869nm) from MODIS Aqua 8-day area averaged for the region 141.02°E, 47.98°S, 142.98°E, 46.02°S from 2010-2019. g) Mean monthly dust deposition (total wet + dry, mg m^{-2} d^{-1}) estimated from MERRA-2 satellite re-analysis model area averaged for the region 48.00°S 141.88°E, 46.00°S 143.13°E from 2010-2019. h) Mean monthly lithogenic particle flux F_{LithAv} (mg m^{-2} d^{-1}) with white text total days sampled in month.

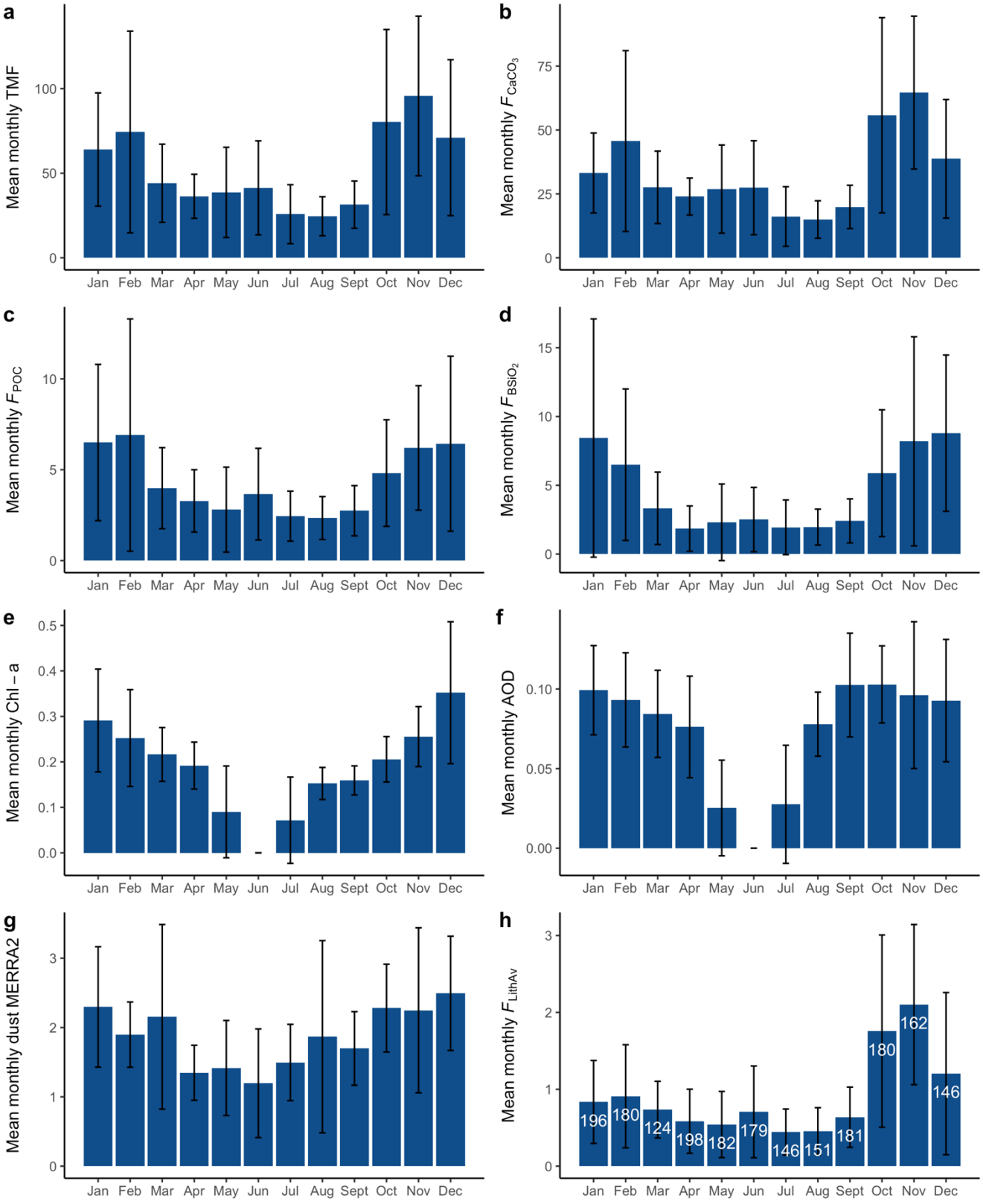
a
Mean monthly TMF
b
Mean monthly F_{CaCO_3}
c
Mean monthly F_{POC}
d
Mean monthly F_{BSiO_2}
e
Mean monthly Chl – a
f
Mean monthly AOD
g
Mean monthly dust MERRA2
h
Mean monthly F_{LithAv}
Jan Feb Mar Apr May Jun Jul Aug Sept Oct Nov Dec
196 180 124 198 182 179 146 151 181 180 162 146

4. Discussion

4.1 – Do lithogenic particle fluxes from SOTS sediment traps reflect the vertical flux of sinking particles?

Sediment traps offer a convenient method of sampling sinking particles in the deep ocean, but questions remain about how well the particle fluxes estimated by sediment traps represent the true vertical particle flux. In particular, conical PARFLUX traps deployed at ~1000m can under collect true sinking fluxes by as much as 60% and over-collect by more than 40% in some regions (Yu et al., 2001). These effects largely arise from a combination of hydrodynamic biases from currents transporting particles in 3-dimensions and hydrodynamic biases of sinking particle due to their composition. However, the relationships between biases and trapping efficiency are non-linear and complex, compounding correction of particle fluxes without specialised analyses using constant flux radiogenic tracers such as ^{230}Th and ^{231}Pa (Scholten et al., 2001; Yu et al., 2001; Buesseler et al., 2007).

Lithogenic particle fluxes at SOTS 1000m depth were treated as a 1-dimensional product of sinking particles through the water column without accounting for advective particle inputs outside the SOTS region (Wynn-Edwards et al., 2020). Our simplification is based on several oceanographic features at SOTS and sediment trap mooring sensor measurements.

SOTS is located within a small anticyclonic gyre formed by the eastward flowing Antarctic Circumpolar Current and the westward flowing temperate subtropical waters to the north outflowing from the East Australian Current (EAC) extension (Rintoul and Trull, 2001; Trull et al., 2001; Herraiz-Borreguero and Rintoul, 2011). Horizontal current velocity measured by the SOTS mooring at 1200m depth averaged 12.29±13.89 cm s^{-1} across the 2010-2018 period (Table 6), which is consistent with earlier observations of decreased advection current speed from the surface to depth (e.g. <15 cm s^{-1} at 1000m by Bray et al. (2000). Wynn-Edwards et al. (2020) estimated that particles collected at 1000m depth at SOTS should be derived from no more than 170km at the surface. This distance indicates the radius of the 'statistical funnel' catchment area of particle flux with depth. The statistical funnel refers to the spatial derivation at the surface of particles trapped at 1000m depth, where >90% of particles collected are derived from the statistical funnel catchment area (Deuser et al., 1990; Siegel and Deuser, 1997; Francois et al., 2002; Siegel et al., 2008).

Table 6. Mean annual horizontal current velocity associated with SOTS sediment traps between 2010 and 2018. No mooring was deployed in 2014. Data obtained from IMOS (portal.aod.org.au)

Deployment year	Mean horizontal velocity (cm s^{-1})	Standard deviation
2010	9.76	13.50
2011	24.13	31.11
2012	10.81	18.56
2013	9.86	6.80
2014	NA	NA
2015	8.65	14.03
2016	7.07	5.44
2017	14.08	9.84
2018	13.98	11.81
Mean	12.29	13.89

Previous sediment traps of the same design placed at 1000m deep at SOTS were subject to low mean tilts of 2.1° (range 1.4° to 4.1°; Bray et al., 2000), indicating collection efficiency of SOTS 1000m traps may not be significantly compromised by lateral currents. As Chiswell and Nodder (2015) point out, the operation of sediment trap collection is based on turbulence generated by the trap mouth, creating small scale eddies and decelerating particles that are intercepted at near horizontal trajectories by the trap funnel (Gardner, 1985; Baker et al., 1988; Siegel and Deuser, 1997). The highly non-linear and unpredictable nature of turbulence dynamics due to current and trap tilt hinders the quantification of current impacts on trapping efficiency (Yu et al., 2001; Honjo et al., 2008; Chiswell and Nodder, 2015). The requirement for trapping efficiency correction factors generated by a complex fluid dynamics model is thus beyond the scope of this study.

Previous examinations of biases associated with moored sediment trap designs indicate that collection is less efficient for shallow traps deployed in high current regions (Yu et al., 2001; Buesseler et al., 2007; Dunne et al., 2007). The use of 1000m depth traps at SOTS in a remote abyssal ocean setting prevents many of the inherent trap biases detailed by Buesseler et al. (2007). Additionally, the use of 1000m traps maintains a reasonable proximity to the ocean surface in view to determine lithogenic particle inputs arising from atmospheric deposition (§4.3.4; Honjo et al., 2008). The depth of 1000m is also required to avoid strong currents that

arise from winter mixing of the water column at SOTS, where the mixed layer depth can be found at >400m depth (Rintoul and Trull, 2001; Trull et al., 2019).

Thus, despite the simplification of particle sinking model to a 1-dimensional framework, consistent trap design and sampling methodology for the duration of the SOTS programme provides reasonable insight into vertical particle flux trends and variability over time.

4.2 – Lithogenic particle flux at SOTS at 1000m depth: characteristics and trends

Lithogenic particle flux estimation at SOTS demonstrated strong seasonality with a peak flux in late spring/early summer followed by a smaller secondary peak in late summer (Figure 4a, b). This two-peak structure was also observed in TMF, $CaCO_3$, POC and opal fluxes (Figure 6a, b, c, d; Figure 7e, f). The two-peak structure of TMF components might be explained by distinct seasonality differences at SOTS due to regular temperate EAC intrusions (sub-tropical surface water) across the STF into the SAZ. Temperate EAC waters have characteristically late winter/spring productivity peaks, while cooler SAZ waters typically exhibit greater productivity in late summer (Trull et al 2001, Rintoul and Trull 2001, Herraiz-Borreguero and Rintoul 2011). F_{LithAv} showed good correlation with TMF (0.841) and $CaCO_3$ flux (0.856), and moderate correlation with POC (0.682) and opal (0.656). This observation may result from particle interaction dynamics between lithogenic and biogeochemical fluxes, or productivity response to nutrient relief, discussed further in §4.6.

Despite clear seasonality in F_{LithAv}, interannual variability was difficult to identify. This is largely due to gaps in the dataset from a lack of trap deployment, insufficient material for analysis or time constraints. Seasons of 2015-16 and 2018-19 demonstrated markedly reduced average seasonal F_{LithAv} compare to earlier seasons, while the 2017-18 season saw a return to higher average F_{LithAv} (Figure 4c). This reduced frequency of higher fluxes was highlighted by slightly lower total average F_{LithAv} of 0.91 mg m^{-2} d^{-1} (all data 2010-2019) measured in our study compared to earlier SOTS seasonal flux estimate of 1.31 mg m^{-2} d^{-1} by Trull et al. (2001) at the end of last century (Table 2). Indeed, some seasonal F_{LithAv} means of 1.5 mg m^{-2} d^{-1} remained high in 2010-11, 2011-12, 2013-14 (Figure 4c)**.** A possible explanation is the large dust storm events of 2002-2003 and 2009 (Gabric et al., 2010; Gabric et al., 2016; O'Loingsigh et al., 2017; De Deckker, 2019) that characterised the so-called "Millennium Drought" between 2000 and 2010 (O'Loingsigh et al., 2017). This prolonged drought period led to enhanced dust

transport and may have caused increased lithogenic material delivery to SOTS early on in the period 2010-2019, subsequently declining throughout the decade with the retreat from drought conditions. Analysis of sediment trap samples from 2001-2010 and dust emission patterns may elucidate the hypothesis of decreasing frequency of high seasonal lithogenic fluxes at SOTS.

4.2.1 – Comparison to ^{230}Th-normalised lithogenic flux from SOTS benthic surface sediments

An estimate of lithogenic flux at SOTS was produced (Weis et al., unpublished) based on ^{230}Th-normalised lithogenic flux (Francois et al., 2004) using benthic sediment core material (Table 2). This surface sediment core top sample (sample ID, IN2018_V02_KC07) was collected at SOTS in 2018 and encompasses approximately 500 years of sediment deposition. The ^{230}Th-normalised lithogenic flux estimate of 1.68±0.08 mg m^{-2} d^{-1} agrees very well with the high end of our seasonal F_{LithAv} estimates of ~1.5 mg m^{-2} d^{-1}. Although higher than the total F_{LithAv} average of 0.91±0.83 mg m^{-2} d^{-1}, the ^{230}Th-normalised flux, which represents a much longer temporal average, remains within the variability of our F_{LithAv} estimate. The agreement between these two methods suggests that ^{230}Th-normalised lithogenic flux from surface sediments is a reliable proxy for mineral dust deposition to the ocean where other lithogenic inputs can be discounted (see §4.3.2). A higher ^{230}Th-normalised lithogenic flux (which was taken at 4474m depth) compared to F_{LithAv} (taken at 1000m depth) may also be caused by lateral sediment inputs, since relative increases in Al-traced lithogenic material with depth have been previously observed at SOTS (Trull et al., 2001).

4.3 – Lithogenic particle elemental composition and provenance

4.3.1 – Biogenic factors influencing lithogenic material

In sinking marine particles, Al, Ti and Th are almost exclusively derived from lithogenic material and thought to have no essential biological utility (Brewer et al., 1980; Otosaka et al., 2004; Boës et al., 2011; Hsieh et al. 2011; Lam and Marchal, 2015; Ohnemus and Lam, 2015; Anderson et al. 2016; Baker et al. 2016; Kienast et al., 2016; Hayes et al. 2017). The terrestrial source of material analysed may originate from regions where lithogenic tracer concentrations deviate from global averaged UCC values (Hsieh et al., 2011; Ohnemus and Lam 2015). The use of multiple lithogenic tracers to determine lithogenic material fluxes aims to reduce

lithogenic flux uncertainty that might be caused by tracer concentrations outside of globally averaged UCC values.

To confirm the appropriate use of Al, Ti, Fe and Th as tracers of lithogenic material arriving at 1000m deep at SOTS, enrichment factors (EFs) and relative correlations between tracers were examined. Elemental enrichment factors were calculated (Equation 7) and compared to global UCC content (Rudnick and Gao, 2003), with EFs approaching 1 indicating a crustal origin for the selected lithogenic tracer. Deviation in crustal material composition from global averages due to regional variability can also result in enrichment factors exceeding 1 (Strzelec et al., 2020). For example, Australian soils, particularly in the western part of the 'red centre' region, are characterised by elevated Fe content, leading to higher Fe/Al ratios compared to northern hemisphere soils (Mahowald et al., 2005; Radhi et al., 2011; Perron et al., 2020a). Another factor influencing elemental EFs in sinking particles is phytoplankton uptake of biologically essential metals such as Fe (Maldonado et al., 2001; Twining and Baines, 2013), resulting in sinking marine particles (detritus and dead cells) enriched in Fe following cell death and zooplankton grazing.

Variability in Fe concentrations in sinking particles warrants investigation since biogenic enrichment and regional crustal source enrichment in Fe may cause deviations from global averaged UCC values. Slight enrichment in Fe relative to Al, Ti and Th was observed compared to global UCC values (Table 4), leading to $F_{Lith,\ Fe}$ being the highest tracer-based lithogenic flux (Figure 3). This apparent enrichment may be due to enriched lithogenic sources compared to the averaged UCC or from different sources of Fe in addition to lithogenic material as discussed below. An improved estimate of lithogenic fluxes at SOTS might be found from using specific UCC content from possible aerosol source regions, since Australian soil characteristically contains a higher Fe/Al ratio compared to global UCC values (Radhi et al., 2011).

$EF_{Fe/Al}$ in SOTS 1000m-deep sediments were examined to determine if biological Fe accumulation was observed. Additionally, correlation of Fe with more refractory lithogenic tracers Al, Ti and Th at SOTS was examined, since Al, Ti and Th do not demonstrate biological utility (Lam and Marchal, 2015; Ohnemus and Lam, 2015; Anderson et al., 2016). High correlation between Fe and Al (0.913), Ti (0.894) and Th (0.846) observed in our study (Table 5, $n = 124$, $p < 0.001$) indicates that Fe in SOTS sediment samples predominantly originates

from lithogenic material. Slight enrichment in Fe relative to Al in SOTS 1000m-deep sediments ($EF_{Fe/Al}$ = 1.12±0.19; Table 4) was typical of Australian soil mineralogy (cf. $EF_{Fe/Al}$ = 1.23 by Kamber et al. (2005); Table 4) rather than biogenic, as plankton reference material BCR-414 displayed higher $EF_{Fe/Al}$ (1.51±0.03). The good correlation between Fe and lithogenic tracers together with relatively low $EF_{Fe/Al}$ in SOTS 1000m-deep sediments compared to biological enrichment suggests that biological accumulation of Fe was not a major component of the lithogenic flux at SOTS across the time series.

Only recently, the pool of authigenic particulate Fe was considered as an important sub-surface source of particulate Fe (Tagliabue et al., 2019). The determination of the authigenic fraction of particulate Fe is outlined by Tagliabue et al. (2019) and requires the assessment of biogenic, lithogenic and authigenic contributions to total particulate Fe. The proportion of lithogenic particulate Fe is determined by compositional gradients of Al, Ti and Th due to their conservation in seawater compared to the crustal source (Hsieh et al., 2011; Ohnemus and Lam 2015). In our study, the good correlation between Fe and Al, Ti and Th (Table 5) suggests that Fe can predominantly be attributed to lithogenic sources in addition to sources described below. Authigenic contributions are thus assumed to be negligible.

4.3.2 – Sub-surface sources of lithogenic material

Lithogenic particles can in theory be delivered to the SOTS site either at the surface, as wind-blown aerosols, or at the subsurface, as current-advected fine-grained sediment. Sub-surface features such as the South Tasman Rise have previously been used to explain potential sources of lithogenic material arriving at SOTS (Cardinal et al., 2001) as well as an increase in lithogenic material observed in 2000 and 3800m depth traps compared to the 1000m trap (Trull et al., 2001). However, the impact of advected particles is expected to be minimal at 1000m depth. Considering the closest continental shelf sediments to SOTS being advected at a moderate average horizontal current velocity of 20 cm s^{-1} (17.3 km d^{-1}; see §4.1), it would take ~29 days to reach SOTS positioned ~500 km away. If a moderate particle sinking velocity of 50 m d^{-1} is used, the arrival of continental shelf sediments at SOTS would approximately occur at ~1500m depth, therefore avoiding the 1000m trap. Thus, the possibility of re-suspended sediment contribution from the South Tasman Rise to particles at SOTS suggested by Cardinal et al. (2001) is highly unlikely, since this continental source is also ~500km east of SOTS and

the south-westerly currents from the EAC extension south of Tasmania are limited (Herraiz-Borreguero and Rintoul 2011).

4.3.3 – Anthropogenic sources of lithogenic material

While the crustal material from Australian soil appears to be the dominant source of lithogenic particles to SOTS, our data suggest anthropogenic sources also contribute. Average Pb enrichment factors of 9.1, 12.4 and 11.9 were found relative to Al, Ti and Th respectively, indicating that anthropogenic emissions contribute significantly to Pb concentration in SOTS 1000m sediments (Table 4). Contributions of anthropogenic sources to V and Pb content is considered significant when the metal's respective enrichment factors exceed 10 (Shelley et al 2017b; Perron et al 2020). Such Pb enrichment relative to Ti, Al and Th was not found in the surface sediment dataset (Weis et al., unpublished) from SOTS (Table 4), likely because this sediment integrates sediment pre-dating significant anthropogenic Pb emissions. SOTS 1000m particle Pb concentrations were found to correlate moderately but significantly to Fe, Al, Ti and Th lithogenic tracer concentrations (0.529, 0.500, 0.528 and 0.608 respectively) in SOTS 1000m particles (Table 5). Thus, the observed enrichment of Pb in SOTS 1000m sinking particles is likely to derive mostly from the same transport mechanism as main lithogenic inputs. Since enrichment of Pb due to anthropogenic sources is highly likely from combustion aerosols, the identification of Pb enrichment and correlation to lithogenic tracers is evidence of both lithogenic and anthropogenic particles arriving at SOTS from aeolian transport mechanisms, as previously suggested by Bowie et al. (2009).

Evidence of anthropogenic TE contributions may also explain slight enrichment in Fe in SOTS 1000m particles relative to lithogenic tracers Al, Ti and Th (EF_{Fe} = 1.12, 1.53, 1.52 respectively), which are unlikely to be from biogenic contributions (cf. EF_{Fe} BCR-414 = 1.51, 2.32, 1.74 respectively, Table 4). This supplementary anthropogenic contribution to lithogenic Fe might explain why $F_{\text{Lith, Fe}}$ produced the largest lithogenic particle flux estimate in Figure 3, outside of deviations in UCC Fe content. This is particularly important, since anthropogenic sources of Fe from combustion aerosols contain a higher fractional Fe solubility than dusts, leading to increased phytoplankton bioavailability (Sholkovitz et al., 2009; Ito et al., 2019).

Particulate Pb emission to the atmosphere in Australia may include combustion of petroleum fuels (Pacyna and Pacyna, 2001; Eyring et al., 2010), traffic from major cities on the southeast coast of Australia, coal-fired energy production, oil and gas industries in the Great Australian

Bight and Bass Strait regions, and metal smelting industry on the coast of Victoria (Pacnya and Pacnya, 2001; Shelley et al., 2017b). Vanadium enrichment in SOTS 1000m sinking particles was only slight (2.5 – 3.5; Table 4) and thus undifferentiated from crustal sources and SOTS surface sediments (KC07 0cm core; Table 4). This lack of anthropogenic V may be due to the little shipping traffic and thus low fuel oil combustion emissions released in proximity to SOTS (Pacnya and Pacnya, 2001; Streibel et al., 2017). Nevertheless, the presence of Pb enrichment in sinking marine sediments is a strong indicator of atmospheric transport and deposition of anthropogenic aerosols to the ocean surface at SOTS.

4.3.4 – Aeolian sources of lithogenic material

$EF_{Fe/Al}$ in SOTS samples of 1.12±0.19 is comparable to Southwest ($EF_{Fe/Al}$ = 1.2±1.2) and Southeast ($EF_{Fe/Al}$ = 1.5±1.2) marine regions of these higher latitudes (Perron et al., 2020). This is indicative that lithogenic material at SOTS may be derived from aerosols of southern Australia, as northern marine regions exhibited comparatively higher $EF_{Fe/Al}$ of 2.2 – 2.5 (Perron et al., 2020) due to the influence of higher $EF_{Fe/Al}$ central Australian 'red' dusts (Kamber et al., 2005; Radhi et al, 2011; Strzelec et al., 2020). Significant anthropogenic tracer enrichment in aerosols was identified by Perron et al., (2020) in both the Southwest and Southeast marine regions (Table 4), providing further evidence for aerosol delivery of Pb (and to some extent, Fe) to SOTS sediments (Table 4).

Further examination of SOTS EFs compared to known Australian mineral dust source EFs (Kamber et al., 2005; Marx et al., 2005b, 2005a; McGowan et al., 2005) suggests mineral dust sources from Southern Australia may explain Ti/Th conservation to the globally average UCC Ti/Th ratio at SOTS. $EF_{Ti/Th}$ in SOTS 1000m sediments of 1.03±0.26 (Table 4) is more aligned with South Australian and north-west Victorian dusts ($EF_{Ti/Th}$ range of 0.88 to 1.16; Marx et al. (2005b, 2005a)) than dust samples from the Darling River in NSW and Queensland average dust composition which show some relative enrichment in Ti/Th ($EF_{Ti/Th}$ of 1.415 and 1.646 respectively; Marx et al., 2005a; Kamber et al., 2005). While the use of EFs to estimate lithogenic material orgin is limited to only 6 tracers here, refinement of more specifc source areas could be achieved using UCC normalised trace metal profiles incorporating the complete suit of trace elements analysed (Marx et al., 2005b, 2005a; Marx and Kamber, 2010).

Dust emission in Australia is highly seasonal, primarily driven by prevailing weather systems. The development of non-precipitation bearing cold front systems throughout the Austral spring is largely responsible for dust transported to the south-eastern seaboard (Ekström et al., 2004; O'Loingsigh et al., 2017). In summer however, the development of the high-pressure systems residing in the Great Australian Bight prevent insurgence of Southern Ocean cold fronts from transporting central Australian dust to higher latitudes (Ekström et al, 2004). Examining these seasonal meteorological patterns in tandem with HYSPLIT back trajectory of dust particles**,** O'loingsigh et al. (2017) suggest that dusts sampled at latitudes higher than 30°S originate from source regions closest to sample sites. Other HYSPLIT back trajectories of aerosol particles arriving at the SOTS site by Bowie et al. (2009) indicates that aeolian particles are derived from open ocean regions, where the prevailing westerly air mass circulation over the Southern Ocean is enriched by Australian dusts. These particle trajectory results from Bowie et al., (2009) and O'loingsigh et al. (2017) suggest dusts arriving at SOTS potentially originate from higher latitude sources closest to SOTS, such as the Eyre peninsula of South Australia (Marx et al., 2005b; McGowan et al., 2005) and Mallee region of northern Victoria (O'Loingsigh et al, 2017; Marx et al., 2005b).

Another indicator of mineral dust being the dominant vector of lithogenic material to SOTS 1000m sediments is the seasonal cycle of F_{LithAv} at SOTS. We consistently observed a late spring-early summer F_{LithAv} peak, occurring between October and December (Figure 7h), which is the expected peak in dust deposition originating from Australia. The typical Australian dust storm season occurs from September through to November (O'Loingsigh et al., 2017; Yu and Ginoux, 2020). This pattern was observed in analysis of AOD data (from MODIS-Aqua RRS at 869nm; NASA Goddard Space Flight Center (2018b)) for the period between 2010 and 2019, which indicated maximum aerosol loading over SOTS occurred in September and October (Figure 7f). Concurrently, model output of dust deposition at SOTS by MERRA-2 satellite shows enhanced aeolian deposition occurs from October through to March, with a peak in December (Figure 7g). Together, this analysis suggests our late spring-early summer F_{LithAv} peak observed at 1000m depth at SOTS may be a direct reflection of Australian dust transport and deposition to the time-series station.

4.4 – Using lithogenic particle flux at 1000m to constrain dust deposition

Our study has made promising steps towards using sinking particles as a proxy for aeolian deposition. Current models of dust deposition such as CAM and MERRA-2 are in good agreement with the variability observed in our estimates of lithogenic particle flux (Table 2; Figure 6g, h). Agreement between our multi-tracer lithogenic flux and ^{230}Th-normalised sediment flux estimates (Weis et al., unpublished) and previous SAZ lithogenic flux estimates (Table 2) by Trull et al. (2001) and Nodder et al. (2016) indicate that the methods used in this study contribute consistent observations to a growing pool of dust deposition estimates in the Southern Ocean. This comparison of multiple approaches reduces the inconsistencies found in all methods of dust deposition (Anderson et al., 2016), aiding the refinement of dust deposition estimates and their variability.

However, there are many factors which can bias estimates of dust deposition at SOTS using marine lithogenic particle flux (F_{LithAv}). The use of 1000m-deep F_{LithAv} as a proxy for dust deposition at SOTS is dependent on a wide range of physical and chemical processes occurring between dust emission at the source and eventual particle trapping at 1000m depth. We show that multi-tracer estimate of F_{LithAv} is more reliable as contributions of Fe from non-lithogenic sources, likely anthropogenic inputs (§4.3.3), can lead to overestimation of F_{LithAv} when only using a Fe as a lithogenic tracer.

For factors affecting sediment trap collection, the estimation of dust deposition from F_{LithAv} relies on the simplification of the process of particle sinking through the water column (§4.1). If we treat F_{LithAv} from sediment traps here purely originating from aeolian deposition with lateral inputs of hemipelagic sediment inputs discounted (§4.3.2), then the F_{LithAv} estimates here indicate an upper limit of dust deposition (Anderson et al., 2016). However, if sediment trapping efficiency is reduced by strong advective currents (Buesseler et al., 2007), aeolian deposition may in reality be under sampled at depth due to sinking particle under-collection (§4.1).

Solubilisation of collected sediment particles in sediment trap cups can result in loss of particle material to the overlying supernatant (Pohl et al., 2004; Antia, 2005; Buesseler et al., 2007). Lithogenic particle flux (F_{LithAv}) estimation from lithogenic particle tracer concentrations may therefore be reduced by dissolution of trace metals in collected particles (Pohl et al., 2004; Antia et al., 2005). However, the dissolution for lithogenic tracers is generally low (e.g. 2% for

Fe, Pohl et al. (2004)) over longer trap deployments when compared to biogenic flux component dissolution (Pohl et al., 2004; Lamborg et al., 2008). Correction for lithogenic particle dissolution has not been made due to the large uncertainties in how to apply corrections to particle mass flux **(**Buesseler et al., 2007) and lack of sediment trap cup supernatant for dissolved particle assessment.

Prior to sediment collection, dissolution of mineral aerosol particles may lead to reduced mass of lithogenic particles reaching 1000m depth, reducing the magnitude of F_{LithAv}. However, processing of the TMF due to aggregation and remineralisation may result in dissolved lithogenic tracers being scavenged by particles. On this effect, Ohnemus and Lam (2015) suggest that Ti provides improved robustness as a lithogenic tracer owing to low reactivity and solubility. Shelley et al. (2017a) also noted low aerosol Ti solubility analysing a range of aerosol types. Th is also considered a robust tracer with respect to dissolution of aeolian particles. Th is highly insoluble in seawater (Hsieh et al., 2011; Hayes et al., 2013) and despite evidence of Th solubility ranging 1 - 23% (Arraes-Mescoff et al., 2001; Roy-Barman et al., 2002), particulate Th solubility is considered very low compared to Fe, where solubility may range orders of magnitude (Mahowald et al., 2005; Sholkovitz et al., 2012). Additionally, the high particle reactive nature of Th means that dissolved concentrations are readily scavenged onto particles (Lam and Marchal, 2015). The use of multiple lithogenic tracers in the calculation of F_{LithAv} allows for differences that may arise due to each tracers' fractional solubility and scavenging potential. Indeed, the good agreement of Al, Ti, Fe and Th traced F_{LithAv} values (Figure 3) delivers a more robust assessment of lithogenic variability due to compounding factors discussed above.

4.5 – Uncertainties associated with lithogenic flux calculation by mass balance

Comparison of F_{LithAv} calculation from multiple lithogenic tracers with that of $F_{\mathrm{Lith,\ MB}}$ estimation from TMF mass balance (§3.2, Equation 6) indicates strong disparity between the two methods used at SOTS, 1000m depth. F_{LithAv} represents 1.7±0.8 % of TMF compared with a $F_{\mathrm{Lith,\ MB}}$ estimate of 8±4 % of TMF (Table 2). Higher correlation between $F_{\mathrm{Lith,\ MB}}$ and POC and opal compared to that between F_{LithAv} and POC and opal together with similarities between the variability of $F_{\mathrm{Lith,\ MB}}$ and TMF fluxes (Figure 5) indicate that $F_{\mathrm{Lith,\ MB}}$ is more associated with export production compared to F_{LithAv}. The use of mass balance to estimate lithogenic flux (Wefer and Fischer, 1993; Ratmeyer et al., 1999a; Ratmeyer et al., 1999b; Francois et al., 2002;

Helmke et al., 2005; Fischer and Karakaş, 2009; Fischer et al., 2009; Nowald et al., 2015; Harms et al., 2021) might therefore overestimate the correlation between lithogenic particles and POC export at 1000m depth. As a consequence, $F_{Lith, MB}$ estimates may exaggerate the role of lithogenic particles in the ballast process of POC (Klaas and Archer, 2002).

On the contrary, our study suggests a small contribution of F_{LithAv} to TMF (1.68±0.77 %), indicating that lithogenic particles do not play a major role in the ballast of POC (Klaas and Archer, 2002) at SOTS. This observation is consistent with open ocean settings where carbonate and biogenic opal are more important physical ballasts of POC than lithogenic material **(**Honjo et al., 2008). While our F_{LithAv} estimates poorly contribution to TMF, it correlates well (0.682) with POC flux (Table 3), which might indicate that lithogenic flux at SOTS is more involved with productivity induction than the physical drive of POC to depth by ballasting (see §4.6.2).

Another factor influencing $F_{Lith, MB}$ estimates lies in the use of the POM:POC relationship in Equation 6. In TMF mass balance calculation, total particulate organic material (POM) is estimated based on the molecular mass of bulk organic material normalised to particulate carbon (POC). Our derivation of $F_{Lith, MB}$ (from Wynn-Edwards et al. (2020) data) uses POM = 2.199´POC (Klaas and Archer, 2002). Francois et al. (2002) and Harms et al. (2021) employ the (Anderson, 1995) empirical marine organic matter formula $C_{106}H_{175}O_{42}N_{16}P$, yielding POM = 1.87´POC (from mean algal elemental composition). The POM:POC ratio may vary regionally due to local phytoplankton taxonomic composition and to nutrient depletion (Suess and Ungerer, 1981; Sharoni and Halevy, 2020). POM:POC ratios should ideally be used at a regional scale where information on both taxonomic composition and nutrient profiles of the water mass are known. Therefore, large uncertainty on the contribution of lithogenic particles to TMF may stem from mass balance calculations due to the use of poorly constrained POM:POC ratios. Indeed, when applying a back calculation to mass balance-based $F_{Lith,MB}$ calculation (Equation 6**)** using our obtained F_{LithAv}, we find a POM:POC ratio of 3.07±0.53. Based on previously used marine organic matter elemental ratios ~2, this value is probably unrealistic as it would imply significantly higher organic material molecular weight than previously reported (Anderson et al., 1995). Alternatively, authigenic particle contributions (e.g. barite; Ohnemus and Lam (2015)) to TMF may also perturb derivation of lithogenic flux by mass balance, and may explain the POM:POC coefficient of 3.07 obtained.

The complex dynamics and composition of particle fluxes indicates that the use of lithogenic particle flux calculation by mass balance can add much more uncertainty than the use of our multi-tracer approach. This study highlights that representation of lithogenic flux trends (e.g. Figure 5) can be subjected to large biases, challenging accurate assessment of the contribution of lithogenic material to trace nutrient inputs and particle ballast. Since multiple factors such as particulate organic matter composition, biological community structure and nutrient availability enter into play to determine particulate organic mass composition, the estimate of lithogenic particles based on lithogenic tracers (Al, Ti and Th) appears to be a more robust and simple method.

4.6 – Lithogenic and biogeochemical component flux at 1000m depth characteristics

4.6.1 – TMF component correlations: particle dynamics

There are many factors that may influence the strong correlation of F_{LithAv} with TMF component fluxes at depth (Table 3), where highest correlation of F_{LithAv} was observed with carbonate flux (0.856; $p<0.001$). Processes including remineralization, scavenging and aggregation/disaggregation result in the substantially altered composition of particles arriving at 1000m depth compared to particles arriving or produced at the ocean surface (Arraes-Mescoff et al., 2001; Lam and Marchal, 2015; Wilks et al., 2017). The mechanisms that may lead to apparent association of lithogenic and biogeochemical fluxes are discussed only briefly, since investigations into these complex processes are beyond the scope of this study.

As discussed in §4.3.4, lithogenic material at SOTS is primarily thought to be sourced by atmospheric deposition of mineral dust (likely from Australia). The comparatively small size (<63 μm) of mineral dust particles (Mahowald et al., 2014) deposited to the ocean surface may result in slower sinking rate compared to larger biogenic particles, leading to prolonged residence time in the euphotic zone (Buesseler et al., 2007; Ebersbach et al., 2011). Scavenging of lithogenic material by larger, faster sinking carbonate rich particles, such as faecal pellets dominated by coccolithophores (Fischer et al., 2009; Rigual Hernández et al., 2020) may entrain lithogenic material into the particulate $CaCO_3$ flux (Balistrieri et al., 1981). This mechanistic association of carbonate and lithogenic material by scavenging is likely responsible for the strong correlation observed between lithogenic and carbonate fluxes (Table 3).

At SOTS, the peak in dust deposition, which follows the onset of the Australian dust storm season (O'Loingsigh et al., 2017; §4.3.4), occurs prior to peak carbonate production (Figure 7f). This may explain why late summer F_{LithAv} peaks are reduced compared to earlier spring peaks (Figure 6h), as scavenging by carbonates reduces the inventory of particulate trace metals. Variability in the magnitude and timing of these seasonal flux peaks (Figure 6) might be further explained by influence of different water masses on productivity at SOTS. Productivity arising from subtropical temperate water in early spring followed by SAZ waters in later summer (§4.1; Trull et al 2001) may cause differences in particle composition (ie. $CaCO_3$:POC:$BSiO_2$ ratio, Figure 6), altering the degree of lithogenic material scavenging. For example, Th has been shown to have increased particle affinity for higher carbonate concentration and decreased affinity in higher opal concentration particles (Chase et al., 2002).

4.6.2 – Lithogenic particle flux at SOTS 1000m depth, dust deposition and productivity

An additional mechanism that may also explain the strong F_{LithAv} correlation to carbonate flux is that of productivity response is directly related to aerosol deposition in the Fe limited waters of the SAZ (Bowie et al., 2009; Boyd and Ellwood, 2010; Ebersbach et al., 2011). Examples of this effect south east of Australia were observed by Gabric et al. (2010); Gabric et al. (2016), however the latter study pointed out that such marine productivity responses were associated with atypical large dust storm events that occurred during the 2000-2009 'Millennium Drought' period (O'Loingsigh et al., 2017). It might be proposed however, that dust deposition at SOTS, which appears to be small given the magnitude of F_{LithAv}, is sufficient to relieve Fe limitation (Bowie et al., 2009) but only enough to induce small seasonal productivity responses reflected in summer chlorophyll concentrations of 0.3 – 0.6 mg m^{-3} observed in this study (Figure 6e, Figure 7e) and also by Trull et al. (2019). At SOTS, low inputs of lithogenic material from atmospheric deposition may contribute to the absence of high magnitude productivity responses ([Chl-a] >2.5 mg m^{-3}; Yoder et al. (1993)) previously observed in North Atlantic spring phytoplankton blooms (Trull et al., 2019).

Satellite observations of increased surface chlorophyll-a (Chl-a) concentration have previously been used to measure dust delivery enhancement of primary productivity in Australia (Shaw et al., 2008; Gabric et al., 2010; Gabric et al., 2016). At SOTS, mean monthly surface chlorophyll concentration over the study period showed good correlation with both mean monthly AOD (0.843, $p<0.001$) and mean monthly MERRA-2 estimates of dust deposition (0.861, $p<0.001$)

(Table 7). Additionally, correlation of mean monthly F_{LithAv} to mean monthly AOD (0.771, p = 0.003) and mean monthly MERRA-2 modelled dust deposition (0.637, p = 0.026) (Table 7). At depth, moderately strong and significant correlation observed between F_{LithAv} and POC flux (0.682, p<0.001) as well as BiSO2 (0.656, p<0.001) fluxes in addition to high F_{LithAv} and $CaCO_3$ correlation (0.856, p<0.001) suggests a general association of export production and F_{LithAv} (Table 3). Evidence of exported POC coupling to surface productivity was found in significant correlation of mean monthly POC flux at 1000m depth to mean monthly surface Chl-a over the study period (0.771, p = 0.003). However, a decoupling of primary productivity stimulation by Fe-bearing aerosol and lithogenic particle flux at depth was evidenced by the insignificant correlation (0.493, p = 0.104) between mean monthly F_{LithAv} and mean monthly surface chlorophyll (Table 7) over the study analysis period.

Table 7. Correlation matrix using Pearson's correlation value (*r*) for mean monthly trends across the study period in F_{LithAv}, AOD, MERRA-2 dust deposition, surface Chl-a concentration and POC flux (F_{POC}) at 1000m depth. Values for statistical significance (p) are given in parentheses. Significant correlations (p < 0.05) in bold (n=12).

	F_{LithAv}	AOD	MERRA-2	Chl-a	F_{POC}
F_{LithAv}	1	-	-	-	-
AOD	0.477 (p=0.117)	1	-	-	-
MERRA-2	**0.637** (p=0.026)	**0.772** (p=0.003)	1	-	-
Chl-a	0.493 (p=0.104)	**0.843** (p<0.001)	**0.861** (p<0.001)	1	-
F_{POC}	**0.635** (p=0.026)	0.521 (p=0.083)	**0.696** (p=0.012)	**0.771** (p=0.003)	1

The correlation between mean monthly surface Chl-a and mean monthly POC exported to depth at SOTS (Table 7) suggests a link between marine productivity and POC export within average annual cycles over the study period. This finding does not however indicate integrated surface productivity and POC export to depth relationships between years. In this regard, Ebersbach et al. (2011) suggested that primary production (gross and net) and exported carbon flux measurements at SOTS are not linearly correlated. This hypothesis was echoed by Wynn-Edwards et al. (2020) who found no correlation between integrated annual net primary production and integrated annual POC export at 1000m depth using the same samples examined in this study over a longer study period.

Examining this discrepancy, Ebersbach et al. (2011) suggested that zooplankton are an important control on export production. Shipboard incubation experiments during the summer 2007 SAZ-Sense cruise indicated high (>80%) primary production removal rates at SOTS by grazers (Pearce et al., 2011)**,** resulting in substantial contribution from faecal aggregate to particle sinking fluxes out of the mixed layer (Ebersbach et al., 2011). Subsequently, very low concentrations of unprocessed phytoplankton material even at relatively shallow (150m) depths at SOTS indicate that secondary productivity consumption of sinking particle flux is an important consideration when examining deep particulate export production correlation to surface productivity (Ebersbach et al., 2011). Thus, any coupling of lithogenic particle fluxes and primary production induced by Fe fertilization is mediated by processes (scavenging, POC remineralization, aggregation/disaggregation cycles; Lam and Marchal, 2015) that alter the composition of particles prior to interception of the sinking particle flux at 1000m (Wynn-Edwards et al., 2020). The linear correlation of lithogenic flux at depth with primary productivity markers like surface Chl-a concentration may therefore be oversimplistic, since aforementioned controls on particle export may temporally decouple lithogenic particles arriving at the surface and those arriving at depth.

Further validation of primary productivity fertilization by mineral dust deposition at SOTS (Bowie et al., 2009) therefore requires mechanistic analyses to consolidate remotely sensed observations and particles collected beyond the mesopelagic zone. Importantly, the quantification of soluble Fe delivered to the Southern Ocean from aerosols (Ito et al., 2020b; Perron et al., 2020b) and further incubation experiments examining Fe and major nutrient limitation (Hassler et al., 2014) are required to determine if aerosol inputs of Fe are sufficient to provide observed Fe inventories and cycles in the SAZ (Bowie et al., 2009). This information is also suggested by Cosentino et al. (2020) as essential for use in methods of correlated dust deposition and satellite estimates of productivity, building on the advice of Boyd et al. (2010) who caution against inferring dust induced productivity using biological signatures such as Chl-a.

5. Conclusions

Analysis of multiple metals (Al, Ti, Fe and Th) as tracers of lithogenic input to seawater was applied to estimate the downward flux of lithogenic material using sinking sediments collected at 1000m depth at the Southern Ocean Time-Series sampling station (SOTS). Our results

demonstrated that, while all four lithogenic flux estimates were in good agreement, the averaged multi-tracer approach reduced uncertainties associated with a single element's reactivity in seawater and concentration in source material. For example, regions where biogenic processes or anthropogenic emissions are elevated may require the use of more conservative metals such as Al, Ti and Th over Fe, since Fe is subject to biological uptake and sources additional to lithogenic material. Al, Ti and Th measured in 1000m-deep sediments at SOTS were attributed only to crustal origin as evidenced by enrichment factors close to 1 (relative to the average global UCC), while slightly enriched Fe content in sinking particles indicated a possibility of secondary anthropogenic contributions in addition to lithogenic material. Additional evidence of anthropogenic contributions to 1000m sinking particles collected at SOTS was highlighted by significant enrichment in Pb (EF_{Pb}>10) measured in our samples (relative to the average global UCC content).

The multi-tracer lithogenic flux estimate, F_{LithAv}, exhibited strong seasonality, with two peaks occurring in spring and in late summer. This seasonality was similar to that of TMF and its components, in particular the seasonal variability of carbonate flux which showed strong correlation with F_{LithAv}. Our multi-tracer lithogenic flux estimate was comparable in magnitude to previous estimates at SOTS and in the SAZ south east of NZ using Al as a single lithogenic tracer. More recent lithogenic flux estimates at SOTS using mass balance calculation suggested a substantially higher value compared to F_{LithAv} estimated in this study. However, we argue that lithogenic flux estimates based on mass balance may overestimate the downward flux of crustal material due to several factors, including exclusion of authigenic particle contributions to total particle mass and assumptions on the POM:POC ratio involved in the calculus. This is especially important for HNLC ocean regions where lithogenic flux is small and nutrients delivered by lithogenic material may be important for productivity, such as in the Southern Ocean.

The F_{LithAv} estimates were slightly smaller yet comparable in magnitude compared to global community atmosphere models and satellite re-analysis models of dust deposition. Inherent biases in the sediment sampling techniques when using sediment traps may underestimate lithogenic fluxes compared to other proxies such as the ^{230}Th-normalised sediment method or lithogenic fluxes estimated by models. Alternatively, the strong variation in seasonality may result from lower average lithogenic flux over the study period when compared to previous

estimates and long-term averages like the ^{230}Th-normalised sediment estimate. Further average lithogenic particle flux may be confirmed by analysis over additional time periods.

Across the study period, peak atmospheric aerosol loading at SOTS from satellite observations coincided with typical dust storm seasonality in Australia, followed by maximum modelled dust deposition from MERRA-2 satellite reanalysis model. These observations preceded the main peak in lithogenic particle flux obtained at 1000m, indicating that lithogenic material in 1000m-deep SOTS sediments could originate from aeolian deposition. Comparison of enrichment factors in SOTS 1000m sediments with Australian dust sources and aerosols collected over southern Australian marine regions indicated that dust sources from South Australia and the Mallee region of Victoria/New South Wales may contribute to 1000m-deep lithogenic sinking material at SOTS.

Average atmospheric loading and modelled dust deposition showed good correlation with surface chlorophyll concentrations. However, no clear linear relationship was found between surface chlorophyll concentration and F_{LithAv} measured at depth at SOTS. This was despite good correlation of surface chlorophyll concentration to POC flux at 1000m and good correlation of F_{LithAv} with POC flux at 1000m within annual cycles. These findings indicate a complex relationship between lithogenic flux and productivity enhancement by dust deposition which may be oversimplified when using particles collected at depth.

Additional work is required to confirm or reject the hypothesis that dust mediates primary productivity in the SAZ south of Tasmania. Evidence of lithogenic particles being transported to SOTS via the atmosphere may require further analysis of sediment samples collected at SOTS at 2000m and 3800m depth. Although these deeper traps are possibly subject to lateral inputs of sub-surface lithogenic material, they would provide additional information on particle processing in the bathypelagic zone. Improved lithogenic material source apportionment may be achieved by comparing SOTS particulate material to genuine soil measurement from suggested source regions within Australia using additional trace metals for increased rigorousness. Finally, analysis of lithogenic tracers in aerosols collected during several voyages to SOTS moorings would shed light on the local atmospheric composition above the sea surface. Overall, a multi-disciplinary approach is essential to fully understand the link between atmospheric composition and deposition with marine productivity and export production to depths at SOTS and in general, in the SAZ.

6. References

Acker, J. G., & Leptoukh, G. (2007). Online Analysis Enhances Use of NASA Earth Science Data. *Eos, Transactions American Geophysical Union*, *88*(2). https://doi.org/10.1029/2007eo020003

Albani, S., Mahowald, N. M., Perry, A. T., Scanza, R. A., Zender, C. S., Heavens, N. G., Maggi, V., Kok, J. F., & Otto-Bliesner, B. L. (2014). Improved dust representation in the Community Atmosphere Model. *Journal of Advances in Modeling Earth Systems*, *6*(3), 541-570. https://doi.org/10.1002/2013MS000279

Anderson, L. A. (1995). On the hydrogen and oxygen content of marine phytoplankton. *Deep Sea Research Part I: Oceanographic Research Papers*, *42*(9), 1675-1680. https://doi.org/https://doi.org/10.1016/0967-0637(95)00072-E

Anderson, R. F., Cheng, H., Edwards, R. L., Fleisher, M. Q., Hayes, C. T., Huang, K. F., Kadko, D., Lam, P. J., Landing, W. M., Lao, Y., Lu, Y., Measures, C. I., Moran, S. B., Morton, P. L., Ohnemus, D. C., Robinson, L. F., & Shelley, R. U. (2016). How well can we quantify dust deposition to the ocean? [Article]. *Philosophical Transactions of the Royal Society A: Mathematical, Physical and Engineering Sciences*, *374*(2081), Article 20150285. https://doi.org/10.1098/rsta.2015.0285

Antia, A. N. (2005). Solubilization of particles in sediment traps: revising the stoichiometry of mixed layer export. *Biogeosciences*, *2*(2), 189-204. https://doi.org/10.5194/bg-2-189-2005

Arraes-Mescoff, R., Roy-Barman, M., Coppola, L., Souhaut, M., Tachikawa, K., Jeandel, C., Sempéré, R., & Yoro, C. (2001). The behavior of Al, Mn, Ba, Sr, REE and Th isotopes during in vitro degradation of large marine particles. *Marine Chemistry*, *73*(1), 1-19. https://doi.org/https://doi.org/10.1016/S0304-4203(00)00065-7

Baker, A. R., Landing, W. M., Bucciarelli, E., Cheize, M., Fietz, S., Hayes, C. T., Kadko, D., Morton, P. L., Rogan, N., Sarthou, G., Shelley, R. U., Shi, Z., Shiller, A., & van Hulten, M. M. P. (2016). Trace element and isotope deposition across the air–sea interface: progress and research needs. *Philosophical Transactions of the Royal Society A: Mathematical, Physical and Engineering Sciences*, *374*(2081), 20160190. https://doi.org/10.1098/rsta.2016.0190

Baker, E. T., Milburn, H. B., & Tennant, D. A. (1988). Field assessment of sediment trap efficiency under varying flow conditions. *Journal of Marine Research*, *46*(3), 573-592.

Balistrieri, L., Brewer, P. G., & Murray, J. W. (1981). Scavenging residence times of trace metals and surface chemistry of sinking particles in the deep ocean. *Deep Sea Research Part A. Oceanographic Research Papers*, *28*(2), 101-121. https://doi.org/https://doi.org/10.1016/0198-0149(81)90085-6

Boës, X., Rydberg, J., Martinez-Cortizas, A., Bindler, R., & Renberg, I. (2011). Evaluation of conservative lithogenic elements (Ti, Zr, Al, and Rb) to study anthropogenic element enrichments in lake sediments. *Journal of Paleolimnology*, *46*, 75-87. https://doi.org/10.1007/s10933-011-9515-z

Bowie, A. R., Lannuzel, D., Remenyi, T. A., Wagener, T., Lam, P. J., Boyd, P. W., Guieu, C., Townsend, A. T., & Trull, T. W. (2009). Biogeochemical iron budgets of the Southern Ocean south of Australia: Decoupling of iron and nutrient cycles in the subantarctic zone by the summertime supply. *Global Biogeochemical Cycles*, *23*(4).

Bowie, A. R., Townsend, A. T., Lannuzel, D., Remenyi, T. A., & van der Merwe, P. (2010). Modern sampling and analytical methods for the determination of trace elements in marine particulate material using magnetic sector inductively coupled plasma–mass spectrometry. *Analytica Chimica Acta*, *676*(1), 15-27. https://doi.org/https://doi.org/10.1016/j.aca.2010.07.037

Boyd, P. W., & Ellwood, M. J. (2010). The biogeochemical cycle of iron in the ocean [Article]. *Nature Geoscience*, *3*(10), 675-682. https://doi.org/10.1038/ngeo964

Boyd, P. W., Jickells, T., Law, C. S., Blain, S., Boyle, E. A., Buesseler, K. O., Coale, K. H., Cullen, J. J., de Baar, H. J. W., Follows, M., Harvey, M., Lancelot, C., Levasseur, M., Owens, N. P. J., Pollard, R., Rivkin, R. B., Sarmiento, J., Schoemann, V., Smetacek, V., Takeda, S., Tsuda, A., Turner, S., & Watson, A. J. (2007). Mesoscale Iron Enrichment Experiments 1993-2005: Synthesis and Future Directions. *Science*, *315*(5812), 612. https://doi.org/10.1126/science.1131669

Boyd, P. W., Mackie, D. S., & Hunter, K. A. (2010). Aerosol iron deposition to the surface ocean — Modes of iron supply and biological responses. *Marine Chemistry*, *120*(1), 128-143. https://doi.org/https://doi.org/10.1016/j.marchem.2009.01.008

Bray, S. G., Trull, T. W., & Manganini, S. J. (2000). SAZ Project Moored Sediment Traps: Results of the 1997-1998 Deployments [Report]. *Antarctic Cooperative Research Centre Reports*(15). (Hobart, Australia)

Brewer, P., Nozaki, Y., Spencer, D. W., & Fleer, A. (1980). Sediment trap experiments in the deep north Atlantic: isotopic and elemental fluxes.

Browning, T. J., Bouman, H. A., Henderson, G. M., Mather, T. A., Pyle, D. M., Schlosser, C., Woodward, E. M. S., & Moore, C. M. (2014). Strong responses of Southern Ocean phytoplankton communities to volcanic ash. *Geophysical Research Letters*, *41*(8), 2851-2857. https://doi.org/10.1002/2014gl059364

Buck, C. S., Aguilar-Islas, A., Marsay, C., Kadko, D., & Landing, W. M. (2019). Trace element concentrations, elemental ratios, and enrichment factors observed in aerosol samples collected during the US GEOTRACES eastern Pacific Ocean transect (GP16) [Article]. *Chemical Geology*, *511*, 212-224. https://doi.org/10.1016/j.chemgeo.2019.01.002

Buesseler, K., Antia, A., Chen, M., Fowler, S., Gardner, W., Gustafsson, O., Harada, K., Michaels, A., Loeff, M., Sarin, M. M., Steinberg, D., & Trull, T. (2007). An assessment of the use of sediment traps for estimating upper ocean particle fuxes. *Journal of Marine Research*, *65*. https://doi.org/10.1357/002224007781567621

Bullard, J. E., Baddock, M., Bradwell, T., Crusius, J., Darlington, E., Gaiero, D., Gassó, S., Gisladottir, G., Hodgkins, R., McCulloch, R., McKenna-Neuman, C., Mockford, T., Stewart, H., & Thorsteinsson, T. (2016). High-latitude dust in the Earth system [Review]. *Reviews of Geophysics*, *54*(2), 447-485. https://doi.org/10.1002/2016RG000518

Cardinal, D., Dehairs, F., Cattaldo, T., & André, L. (2001). Geochemistry of suspended particles in the Subantarctic and Polar Frontal zones south of Australia: Constraints on export and advection processes. *Journal of Geophysical Research: Oceans*, *106*(C12), 31637-31656. https://doi.org/10.1029/2000JC000251

Chase, Z., Anderson, R. F., Fleisher, M. Q., & Kubik, P. W. (2002). The influence of particle composition and particle flux on scavenging of Th, Pa and Be in the ocean. *Earth and Planetary Science Letters*, *204*(1), 215-229. https://doi.org/https://doi.org/10.1016/S0012-821X(02)00984-6

Chiswell, S. M., & Nodder, S. D. (2015). Tilt-induced biases in sediment trap functioning. *Journal of Geophysical Research: Oceans*, *120*(12), 8381-8391. https://doi.org/https://doi.org/10.1002/2015JC011350

Cosentino, N. J., Ruiz-Etcheverry, L. A., Bia, G. L., Simonella, L. E., Coppo, R., Torre, G., Saraceno, M., Tur, V. M., & Gaiero, D. M. (2020). Does Satellite Chlorophyll-a Respond to Southernmost Patagonian Dust? A Multi-year, Event-Based Approach. *Journal of Geophysical Research: Biogeosciences*, *125*(12). https://doi.org/10.1029/2020jg006073

De Deckker, P. (2019). An evaluation of Australia as a major source of dust. *Earth-Science Reviews*, *194*, 536-567. https://doi.org/10.1016/j.earscirev.2019.01.008

Deuser, W. G., Muller-Karger, F. E., Evans, R. H., Brown, O. B., Esaias, W. E., & Feldman, G. C. (1990). Surface-ocean color and deep-ocean carbon flux: how close a connection? *Deep Sea*

Research Part A. Oceanographic Research Papers, *37*(8), 1331-1343. https://doi.org/https://doi.org/10.1016/0198-0149(90)90046-X

Duce, R. A., & Tindale, N. W. (1991). Atmospheric transport of iron and its deposition in the ocean. *Limnology and Oceanography*, *36*(8), 1715-1726. https://doi.org/https://doi.org/10.4319/lo.1991.36.8.1715

Dunne, J. P., Sarmiento, J. L., & Gnanadesikan, A. (2007). A synthesis of global particle export from the surface ocean and cycling through the ocean interior and on the seafloor [Article]. *Global Biogeochemical Cycles*, *21*(4), Article Gb4006. https://doi.org/10.1029/2006GB002907

Durand, A., Chase, Z., Noble, T. L., Bostock, H., Jaccard, S. L., Kitchener, P., Townsend, A. T., Jansen, N., Kinsley, L., Jacobsen, G., Johnson, S., & Neil, H. (2017). Export production in the New-Zealand region since the Last Glacial Maximum [Article]. *Earth and Planetary Science Letters*, *469*, 110-122. https://doi.org/10.1016/j.epsl.2017.03.035

Dymond, J., Collier, R., McManus, J., Honjo, S., & Manganini, S. (1997). Can the aluminum and titanium contents of ocean sediments be used to determine the paleoproductivity of the oceans? *Paleoceanography*, *12*(4), 586-593. https://doi.org/10.1029/97pa01135

Ebersbach, F., Trull, T. W., Davies, D. M., & Bray, S. G. (2011). Controls on mesopelagic particle fluxes in the Sub-Antarctic and Polar Frontal Zones in the Southern Ocean south of Australia in summer—Perspectives from free-drifting sediment traps. *Deep Sea Research Part II: Topical Studies in Oceanography*, *58*(21), 2260-2276. https://doi.org/https://doi.org/10.1016/j.dsr2.2011.05.025

Ekström, M., McTainsh, G. H., & Chappell, A. (2004). Australian dust storms: temporal trends and relationships with synoptic pressure distributions (1960-99). *International Journal of Climatology*, *24*(12), 1581-1599. https://doi.org/10.1002/joc.1072

Eyring, V., Isaksen, I. S. A., Berntsen, T., Collins, W. J., Corbett, J. J., Endresen, O., Grainger, R. G., Moldanova, J., Schlager, H., & Stevenson, D. S. (2010). Transport impacts on atmosphere and climate: Shipping. *Atmospheric Environment*, *44*(37), 4735-4771. https://doi.org/10.1016/j.atmosenv.2009.04.059

Fischer, G., & Karakaş, G. (2009). Sinking rates and ballast composition of particles in the Atlantic Ocean: implications for the organic carbon fluxes to the deep ocean. *Biogeosciences*, *6*(1), 85-102. https://doi.org/10.5194/bg-6-85-2009

Fischer, G., Karakas, G., Blaas, M., Ratmeyer, V., Nowald, N., Schlitzer, R., Helmke, P., Davenport, R., Donner, B., Neuer, S., & Wefer, G. (2009). Mineral ballast and particle settling rates in the coastal upwelling system off NW Africa and the South Atlantic. *International Journal of Earth Sciences*, *98*(2), 281-298. https://doi.org/10.1007/s00531-007-0234-7

Francois, R., Frank, M., Rutgers van der Loeff, M. M., & Bacon, M. P. (2004). 230Th normalization: An essential tool for interpreting sedimentary fluxes during the late Quaternary. *Paleoceanography*, *19*(1). https://doi.org/10.1029/2003PA000939

Francois, R., Honjo, S., Krishfield, R., & Manganini, S. (2002). Factors controlling the flux of organic carbon to the bathypelagic zone of the ocean. *Global Biogeochemical Cycles*, *16*(4), 34-31-34-20. https://doi.org/https://doi.org/10.1029/2001GB001722

Gabric, A. J., Cropp, R., McTainsh, G., Butler, H., Johnston, B. M., O'Loingsigh, T., & Van Tran, D. (2016). Tasman Sea biological response to dust storm events during the austral spring of 2009 [Article]. *Marine and Freshwater Research*, *67*(8), 1090-1102. https://doi.org/10.1071/MF14321

Gabric, A. J., Cropp, R. A., McTainsh, G. H., Johnston, B. M., Butler, H., Tilbrook, B., & Keywood, M. (2010). Australian dust storms in 2002-2003 and their impact on Southern Ocean biogeochemistry. *Global Biogeochemical Cycles*, *24*(2), n/a-n/a. https://doi.org/10.1029/2009gb003541

Gardner, W. D. (1985). The effect of tilt on sediment trap efficiency. *Deep Sea Research Part A. Oceanographic Research Papers*, *32*(3), 349-361. https://doi.org/https://doi.org/10.1016/0198-0149(85)90083-4

Geider, R. J., & Laroche, J. (1994). The role of iron in phytoplankton photosynthesis, and the potential for iron-limitation or primary productivity in the sea. *Photosynthesis Research*, *39*(3), 275-301. https://doi.org/10.1007/bf00014588

Gledhill, M., & Buck, K. N. (2012). The organic complexation of iron in the marine environment: a review. *Frontiers in Microbiology*, *3*, Article 69. https://doi.org/10.3389/fmicb.2012.00069

GMAO. (2015). *MERRA-2 tavgM_2d_adg_Nx: 2d, Monthly mean, Time-averaged, Single-Level, Assimilation, Aerosol Diagnostics (extended) V5.12.4*. https://doi.org/10.5067/RZIK2TV7PP38

Gruber, N., Gloor, M., Mikaloff Fletcher, S. E., Doney, S. C., Dutkiewicz, S., Follows, M. J., Gerber, M., Jacobson, A. R., Joos, F., Lindsay, K., Menemenlis, D., Mouchet, A., Müller, S. A., Sarmiento, J. L., & Takahashi, T. (2009). Oceanic sources, sinks, and transport of atmospheric CO2. *Global Biogeochemical Cycles*, *23*(1), n/a-n/a. https://doi.org/10.1029/2008gb003349

Harms, N. C., Lahajnar, N., Gaye, B., Rixen, T., Schwarz-Schampera, U., & Emeis, K.-C. (2021). Sediment trap-derived particulate matter fluxes in the oligotrophic subtropical gyre of the South Indian Ocean. *Deep Sea Research Part II: Topical Studies in Oceanography*, 104924. https://doi.org/https://doi.org/10.1016/j.dsr2.2020.104924

Hassler, C. S., Ridgway, K. R., Bowie, A. R., Butler, E. C. V., Clementson, L. A., Doblin, M. A., Davies, D. M., Law, C., Ralph, P. J., van der Merwe, P., Watson, R., & Ellwood, M. J. (2014). Primary productivity induced by iron and nitrogen in the Tasman Sea: an overview of the PINTS expedition. *Marine and Freshwater Research*, *65*(6), 517-537. https://doi.org/10.1071/MF13137

Hauck, J., Völker, C., Wolf-Gladrow, D. A., Laufkötter, C., Vogt, M., Aumont, O., Bopp, L., Buitenhuis, E. T., Doney, S. C., Dunne, J., Gruber, N., Hashioka, T., John, J., Quéré, C. L., Lima, I. D., Nakano, H., Séférian, R., & Totterdell, I. (2015). On the Southern Ocean CO2 uptake and the role of the biological carbon pump in the 21st century. *Global Biogeochemical Cycles*, *29*(9), 1451-1470. https://doi.org/10.1002/2015gb005140

Hayes, C. T., Rosen, J., McGee, D., & Boyle, E. A. (2017). Thorium distributions in high- and low-dust regions and the significance for iron supply [https://doi.org/10.1002/2016GB005511]. *Global Biogeochemical Cycles*, *31*(2), 328-347. https://doi.org/https://doi.org/10.1002/2016GB005511

Helmke, P., Romero, O., & Fischer, G. (2005). Northwest African upwelling and its effect on offshore organic carbon export to the deep sea. *Global Biogeochemical Cycles*, *19*(4). https://doi.org/10.1029/2004GB002265

Herraiz-Borreguero, L., & Rintoul, S. R. (2011). Regional circulation and its impact on upper ocean variability south of Tasmania. *Deep Sea Research Part II: Topical Studies in Oceanography*, *58*(21), 2071-2081. https://doi.org/https://doi.org/10.1016/j.dsr2.2011.05.022

Honjo, S., Manganini, S. J., Krishfield, R. A., & Francois, R. (2008). Particulate organic carbon fluxes to the ocean interior and factors controlling the biological pump: A synthesis of global sediment trap programs since 1983 [Article]. *Progress in Oceanography*, *76*(3), 217-285. https://doi.org/10.1016/j.pocean.2007.11.003

Hsieh, Y.-T., Henderson, G. M., & Thomas, A. L. (2011). Combining seawater 232Th and 230Th concentrations to determine dust fluxes to the surface ocean. *Earth and Planetary Science Letters*, *312*(3), 280-290. https://doi.org/https://doi.org/10.1016/j.epsl.2011.10.022

Hunter, K. A., & Boyd, P. W. (2007). Iron-binding ligands and their role in the ocean biogeochemistry of iron. *Environmental Chemistry*, *4*(4), 221-232. https://doi.org/10.1071/EN07012

Ito, A., Myriokefalitakis, S., Kanakidou, M., Mahowald, N. M., Scanza, R. A., Hamilton, D. S., Baker, A. R., Jickells, T., Sarin, M., Bikkina, S., Gao, Y., Shelley, R. U., Buck, C. S., Landing, W. M., Bowie, A. R., Perron, M. M. G., Guieu, C., Meskhidze, N., Johnson, M. S., Feng, Y., Kok, J. F., Nenes, A., & Duce, R. A. (2019). Pyrogenic iron: The missing link to high iron solubility in aerosols. *Science Advances*, *5*(5), eaau7671. https://doi.org/10.1126/sciadv.aau7671

Ito, A., Perron, M. M. G., Proemse, B. C., Strzelec, M., Gault-Ringold, M., Boyd, P. W., & Bowie, A. R. (2020a). Evaluation of aerosol iron solubility over Australian coastal regions based on inverse modeling: implications of bushfires on bioaccessible iron concentrations in the Southern Hemisphere. *Progress in Earth and Planetary Science*, *7*(1). https://doi.org/10.1186/s40645-020-00357-9

Ito, A., Ye, Y., Yamamoto, A., Watanabe, M., & Aita, M. N. (2020b). Responses of ocean biogeochemistry to atmospheric supply of lithogenic and pyrogenic iron-containing aerosols [Article]. *Geological Magazine*, *157*(5), 741-756. https://doi.org/10.1017/S0016756819001080

Jickells, T., An, Z. S., Andersen, K. K., Baker, A. R., Bergametti, G., Brooks, N., Cao, J. J., Boyd, P. W., Duce, R. A., Hunter, K. A., Kawahata, H., Kubilay, N., laRoche, J., Liss, P. S., Mahowald, N., Prospero, J. M., Ridgwell, A. J., Tegen, I., & Torres, R. (2005). Global iron connections between desert dust, ocean biogeochemistry, and climate. *Science*, *308*(5718), 67-71. https://doi.org/10.1126/science.1105959

Jickells, T., & Moore, C. M. (2015). The Importance of Atmospheric Deposition for Ocean Productivity. *Annual Review of Ecology, Evolution, and Systematics*, *46*(1), 481-501. https://doi.org/10.1146/annurev-ecolsys-112414-054118

Kamber, B. S., Greig, A., & Collerson, K. D. (2005). A new estimate for the composition of weathered young upper continental crust from alluvial sediments, Queensland, Australia. *Geochimica et Cosmochimica Acta*, *69*(4), 1041-1058. https://doi.org/10.1016/j.gca.2004.08.020

Khatiwala, S., Primeau, F., & Hall, T. (2009). Reconstruction of the history of anthropogenic CO2 concentrations in the ocean. *Nature*, *462*(7271), 346-349. https://doi.org/10.1038/nature08526

Kienast, S. S., Winckler, G., Lippold, J., Albani, S., & Mahowald, N. M. (2016). Tracing dust input to the global ocean using thorium isotopes in marine sediments: ThoroMap. *Global Biogeochemical Cycles*, *30*(10), 1526-1541. https://doi.org/10.1002/2016GB005408

Klaas, C., & Archer, D. (2002). Association of sinking organic matter with various types of mineral ballast in the deep sea: Implications for the rain ratio. *Global Biogeochemical Cycles, v.16, art. no.-1116 (2002)*, *16*. https://doi.org/10.1029/2001GB001765

Lam, P. J., & Marchal, O. (2015). Insights into Particle Cycling from Thorium and Particle Data. *Annual Review of Marine Science*, *7*(1), 159-184. https://doi.org/10.1146/annurev-marine-010814-015623

Lamborg, C. H., Buesseler, K. O., & Lam, P. J. (2008). Sinking fluxes of minor and trace elements in the North Pacific Ocean measured during the VERTIGO program. *Deep Sea Research Part II: Topical Studies in Oceanography*, *55*(14-15), 1564-1577. https://doi.org/10.1016/j.dsr2.2008.04.012

Lauderdale, J. M., Williams, R. G., Munday, D. R., & Marshall, D. P. (2017). The impact of Southern Ocean residual upwelling on atmospheric CO2 on centennial and millennial timescales. *Climate Dynamics*, *48*(5), 1611-1631. https://doi.org/10.1007/s00382-016-3163-y

Li, F., Ginoux, P., & Ramaswamy, V. (2008). Distribution, transport, and deposition of mineral dust in the Southern Ocean and Antarctica: Contribution of major sources. *Journal of Geophysical Research*, *113*(D10). https://doi.org/10.1029/2007jd009190

Luo, C., Mahowald, N., Bond, T., Chuang, P. Y., Artaxo, P., Siefert, R., Chen, Y., & Schauer, J. (2008). Combustion iron distribution and deposition. *Global Biogeochemical Cycles*, *22*(1), n/a-n/a. https://doi.org/10.1029/2007gb002964

Maher, B. A., Prospero, J. M., Mackie, D., Gaiero, D., Hesse, P. P., & Balkanski, Y. (2010). Global connections between aeolian dust, climate and ocean biogeochemistry at the present day and at the last glacial maximum. *Earth-Science Reviews*, *99*(1), 61-97. https://doi.org/https://doi.org/10.1016/j.earscirev.2009.12.001

Mahowald, N., Albani, S., Kok, J. F., Engelstaeder, S., Scanza, R., Ward, D. S., & Flanner, M. G. (2014). The size distribution of desert dust aerosols and its impact on the Earth system. *Aeolian Research*, *15*, 53-71. https://doi.org/https://doi.org/10.1016/j.aeolia.2013.09.002

Mahowald, N. M., Baker, A. R., Bergametti, G., Brooks, N., Duce, R. A., Jickells, T. D., Kubilay, N., Prospero, J. M., & Tegen, I. (2005). Atmospheric global dust cycle and iron inputs to the ocean. *Global Biogeochemical Cycles*, *19*(4). https://doi.org/10.1029/2004GB002402

Mahowald, N. M., Engelstaedter, S., Luo, C., Sealy, A., Artaxo, P., Benitez-Nelson, C., Bonnet, S., Chen, Y., Chuang, P. Y., Cohen, D. D., Dulac, F., Herut, B., Johansen, A. M., Kubilay, N., Losno, R., Maenhaut, W., Paytan, A., Prospero, J. M., Shank, L. M., & Siefert, R. L. (2009). Atmospheric Iron Deposition: Global Distribution, Variability, and Human Perturbations. *Annual Review of Marine Science*, *1*(1), 245-278. https://doi.org/10.1146/annurev.marine.010908.163727

Mahowald, N. M., Muhs, D. R., Levis, S., Rasch, P. J., Yoshioka, M., Zender, C. S., & Luo, C. (2006). Change in atmospheric mineral aerosols in response to climate: Last glacial period, preindustrial, modern, and doubled carbon dioxide climates. *Journal of Geophysical Research: Atmospheres*, *111*(D10). https://doi.org/10.1029/2005jd006653

Maldonado, M. T., Boyd, P. W., LaRoche, J., Strzepek, R., Waite, A., Bowie, A. R., Croot, P. L., Frew, R. D., & Price, N. M. (2001). Iron uptake and physiological response of phytoplankton during a mesoscale Southern Ocean iron enrichment. *Limnology and Oceanography*, *46*(7), 1802-1808. https://doi.org/https://doi.org/10.4319/lo.2001.46.7.1802

Marinov, I., Gnanadesikan, A., Toggweiler, J. R., & Sarmiento, J. L. (2006). The Southern Ocean biogeochemical divide. *Nature*, *441*(7096), 964-967. https://doi.org/10.1038/nature04883

Marshall, J., & Speer, K. (2012). Closure of the meridional overturning circulation through Southern Ocean upwelling. *Nature Geoscience*, *5*(3), 171-180. https://doi.org/10.1038/ngeo1391

Martin, J. H., Gordon, R. M., & Fitzwater, S. E. (1990). Iron in Antarctic waters. *Nature*, *345*(6271), 156-158. https://doi.org/10.1038/345156a0

Marx, S. K., & Kamber, B. S. (2010). Trace-element systematics of sediments in the Murray–Darling Basin, Australia: Sediment provenance and palaeoclimate implications of fine scale chemical heterogeneity. *Applied Geochemistry*, *25*(8), 1221-1237. https://doi.org/https://doi.org/10.1016/j.apgeochem.2010.05.007

Marx, S. K., Kamber, B. S., & McGowan, H. A. (2005a). Estimates of Australian dust flux into New Zealand: Quantifying the eastern Australian dust plume pathway using trace element calibrated 210Pb as a monitor. *Earth and Planetary Science Letters*, *239*(3-4), 336-351. https://doi.org/10.1016/j.epsl.2005.09.002

Marx, S. K., Kamber, B. S., & McGowan, H. A. (2005b). Provenance of long-travelled dust determined with ultra-trace-element composition: a pilot study with samples from New Zealand glaciers. *Earth Surface Processes and Landforms*, *30*(6), 699-716. https://doi.org/10.1002/esp.1169

McGowan, H. A., Kamber, B., McTainsh, G. H., & Marx, S. K. (2005). High resolution provenancing of long travelled dust deposited on the Southern Alps, New Zealand. *Geomorphology*, *69*(1), 208-221. https://doi.org/https://doi.org/10.1016/j.geomorph.2005.01.005

Middag, R., de Baar, H. J. W., Klunder, M. B., & Laan, P. (2013). Fluxes of dissolved aluminum and manganese to the Weddell Sea and indications for manganese co-limitation. *Limnology and Oceanography*, *58*(1), 287-300. https://doi.org/10.4319/lo.2013.58.1.0287

Myriokefalitakis, S., Ito, A., Kanakidou, M., Nenes, A., Krol, M. C., Mahowald, N. M., Scanza, R. A., Hamilton, D. S., Johnson, M. S., Meskhidze, N., Kok, J. F., Guieu, C., Baker, A. R., Jickells, T. D., Sarin, M. M., Bikkina, S., Shelley, R., Bowie, A., Perron, M. M. G., & Duce, R. A. (2018). Reviews and syntheses: The GESAMP atmospheric iron deposition model intercomparison study [Review]. *Biogeosciences*, *15*(21), 6659-6684. https://doi.org/10.5194/bg-15-6659-2018

NASA Goddard Space Flight Center, O. E. L., Ocean Biology Processing Group. (2018a). *Moderate-resolution Imaging Spectroradiometer (MODIS) Aqua Chlorophyll Data; 2018 Reprocessing. NASA OB.DAAC, Greenbelt, MD, USA.* https://doi.org/data/10.5067/AQUA/MODIS/L3M/CHL/2018

NASA Goddard Space Flight Center, O. E. L., Ocean Biology Processing Group. (2018b). *Moderate-resolution Imaging Spectroradiometer (MODIS) Aqua Remote-Sensing Reflectance Data; 2018 Reprocessing. NASA OB.DAAC, Greenbelt, MD, USA*. https://doi.org/data/10.5067/AQUA/MODIS/L3M/RRS/2018

Nodder, S. D., Chiswell, S. M., & Northcote, L. C. (2016). Annual cycles of deep-ocean biogeochemical export fluxes in subtropical and subantarctic waters, southwest Pacific Ocean [Article]. *Journal of Geophysical Research: Oceans*, *121*(4), 2405-2424. https://doi.org/10.1002/2015JC011243

Nowald, N., Iversen, M. H., Fischer, G., Ratmeyer, V., & Wefer, G. (2015). Time series of in-situ particle properties and sediment trap fluxes in the coastal upwelling filament off Cape Blanc, Mauritania. *Progress in Oceanography*, *137*, 1-11. https://doi.org/https://doi.org/10.1016/j.pocean.2014.12.015

O'Loingsigh, T., Chubb, T., Baddock, M., Kelly, T., Tapper, N. J., De Deckker, P., & McTainsh, G. (2017). Sources and pathways of dust during the Australian "Millennium Drought" decade. *Journal of Geophysical Research: Atmospheres*, *122*(2), 1246-1260. https://doi.org/https://doi.org/10.1002/2016JD025737

Ohnemus, D. C., & Lam, P. J. (2015). Cycling of lithogenic marine particles in the US GEOTRACES North Atlantic transect. *Deep Sea Research Part II: Topical Studies in Oceanography*, *116*, 283-302. https://doi.org/https://doi.org/10.1016/j.dsr2.2014.11.019

Otosaka, S., Togawa, O., Baba, M., Karasev, E., Volkov, Y. N., Omata, N., & Noriki, S. (2004). Lithogenic flux in the Japan Sea measured with sediment traps. *Marine Chemistry*, *91*(1), 143-163. https://doi.org/https://doi.org/10.1016/j.marchem.2004.06.006

Pacyna, J. M., & Pacyna, E. G. (2001). An assessment of global and regional emissions of trace metals to the atmosphere from anthropogenic sources worldwide. *Environmental Reviews*, *9*(4), 269-298. https://doi.org/10.1139/a01-012

Pardo, P. C., Tilbrook, B., Langlais, C., Trull, T. W., & Rintoul, S. R. (2017). Carbon uptake and biogeochemical change in the Southern Ocean, south of Tasmania. *Biogeosciences*, *14*(22), 5217-5237. https://doi.org/10.5194/bg-14-5217-2017

Pearce, I., Davidson, A. T., Thomson, P. G., Wright, S., & van den Enden, R. (2011). Marine microbial ecology in the sub-Antarctic Zone: Rates of bacterial and phytoplankton growth and grazing by heterotrophic protists. *Deep Sea Research Part II: Topical Studies in Oceanography*, *58*(21), 2248-2259. https://doi.org/https://doi.org/10.1016/j.dsr2.2011.05.030

Perron, M. M. G., Proemse, B. C., Strzelec, M., Gault-Ringold, M., Boyd, P. W., Rodriguez, E. S., Paull, B., & Bowie, A. R. (2020a). Origin, transport and deposition of aerosol iron to Australian coastal waters [Article]. *Atmospheric Environment*, *228*, Article 117432. https://doi.org/10.1016/j.atmosenv.2020.117432

Perron, M. M. G., Strzelec, M., Gault-Ringold, M., Proemse, B. C., Boyd, P. W., & Bowie, A. R. (2020b). Assessment of leaching protocols to determine the solubility of trace metals in aerosols. *Talanta*, *208*, 120377. https://doi.org/10.1016/j.talanta.2019.120377

Pohl, C., Löffler, A., & Hennings, U. (2004). A sediment trap flux study for trace metals under seasonal aspects in the stratified Baltic Sea (Gotland Basin; 57°19.20′N; 20°03.00′E). *Marine Chemistry*, *84*(3), 143-160. https://doi.org/https://doi.org/10.1016/j.marchem.2003.07.002

Radhi, M., Box, M. A., Box, G. P., Keywood, M. D., Cohen, D. D., Stelcer, E., & Mitchell, R. M. (2011). Size-resolved chemical composition of Australian dust aerosol during winter. *Environmental Chemistry*, *8*(3). https://doi.org/10.1071/en10134

Ratmeyer, V., Balzer, W., Bergametti, G., Chiapello, I., Fischer, G., & Wyputta, U. (1999a). Seasonal impact of mineral dust on deep-ocean particle flux in the eastern subtropical Atlantic Ocean. *Marine Geology*, *159*(1), 241-252. https://doi.org/https://doi.org/10.1016/S0025-3227(98)00197-2

Ratmeyer, V., Fischer, G., & Wefer, G. (1999b). Lithogenic particle fluxes and grain size distributions in the deep ocean off northwest Africa: Implications for seasonal changes of aeolian dust input and downward transport. *Deep Sea Research Part I: Oceanographic Research Papers*, *46*(8), 1289-1337. https://doi.org/https://doi.org/10.1016/S0967-0637(99)00008-4

Rauschenberg, S., & Twining, B. S. (2015). Evaluation of approaches to estimate biogenic particulate trace metals in the ocean [Article]. *Marine Chemistry*, *171*, 67-77. https://doi.org/10.1016/j.marchem.2015.01.004

Rigual Hernández, A. S., Flores, J. A., Sierro, F. J., Fuertes, M. A., Cros, L., & Trull, T. W. (2018). Coccolithophore populations and their contribution to carbonate export during an annual cycle in the Australian sector of the Antarctic zone. *Biogeosciences*, *15*(6), 1843-1862. https://doi.org/10.5194/bg-15-1843-2018

Rigual Hernández, A. S., Trull, T. W., Nodder, S. D., Flores, J. A., Bostock, H., Abrantes, F., Eriksen, R. S., Sierro, F. J., Davies, D. M., Ballegeer, A. M., Fuertes, M. A., & Northcote, L. C. (2020). Coccolithophore biodiversity controls carbonate export in the Southern Ocean. *Biogeosciences*, *17*(1), 245-263. https://doi.org/10.5194/bg-17-245-2020

Rintoul, S. R., & Trull, T. W. (2001). Seasonal evolution of the mixed layer in the Subantarctic zone south of Australia. *Journal of Geophysical Research: Oceans*, *106*(C12), 31447-31462. https://doi.org/https://doi.org/10.1029/2000JC000329

Roy-Barman, M., Coppola, L., & Souhaut, M. (2002). Thorium isotopes in the western Mediterranean Sea: an insight into the marine particle dynamics. *Earth and Planetary Science Letters*, *196*(3), 161-174. https://doi.org/https://doi.org/10.1016/S0012-821X(01)00606-9

Rudnick, R., & Gao, S. (2003). Composition of the Continental Crust. Treatise Geochem 3:1-64. *Treatise on Geochemistry*, *3*, 1-64. https://doi.org/10.1016/B0-08-043751-6/03016-4

Sabine, C. L., Feely, R. A., Gruber, N., Key, R. M., Lee, K., Bullister, J. L., Wanninkhof, R., Wong, C. S., Wallace, D. W., Tilbrook, B., Millero, F. J., Peng, T. H., Kozyr, A., Ono, T., & Rios, A. F. (2004). The oceanic sink for anthropogenic CO2. *Science*, *305*(5682), 367-371. https://doi.org/10.1126/science.1097403

Scholten, J., Fietzke, J., Vogler, S., Loeff, M. M., Mangini, A., Koeve, W., Waniek, J., Stoffers, P., Antia, A., & Kuss, J. (2001). Trapping efficiencies of sediment traps from the deep Eastern North Atlantic: The 230Th calibration. *Deep Sea Research Part II: Topical Studies in Oceanography*, *48*, 2383-2408. https://doi.org/10.1016/S0967-0645(00)00176-4

Shadwick, E. H., Trull, T. W., Tilbrook, B., Sutton, A. J., Schulz, E., & Sabine, C. L. (2015). Seasonality of biological and physical controls on surface ocean CO2from hourly observations at the Southern Ocean Time Series site south of Australia. *Global Biogeochemical Cycles*, *29*(2), 223-238. https://doi.org/10.1002/2014gb004906

Shao, Y., Wyrwoll, K. H., Chappell, A., Huang, J., Lin, Z., McTainsh, G. H., Mikami, M., Tanaka, T. Y., Wang, X., & Yoon, S. (2011). Dust cycle: An emerging core theme in Earth system science [Review]. *Aeolian Research*, *2*(4), 181-204. https://doi.org/10.1016/j.aeolia.2011.02.001

Sharoni, S., & Halevy, I. (2020). Nutrient ratios in marine particulate organic matter are predicted by the population structure of well-adapted phytoplankton. *Science Advances*, *6*(29), eaaw9371. https://doi.org/10.1126/sciadv.aaw9371

Shaw, E. C., Gabric, A. J., & McTainsh, G. H. (2008). Impacts of aeolian dust deposition on phytoplankton dynamics in Queensland coastal waters. *Marine and Freshwater Research*, *59*(11), 951-962. https://doi.org/10.1071/MF08087

Shelley, R., Landing, W., Ussher, S., Planquette, H., & Sarthou, G. (2017a). Characterisation of aerosol provenance from the fractional solubility of Fe (Al, Ti, Mn, Co, Ni, Cu, Zn, Cd and Pb) in North Atlantic aerosols (GEOTRACES cruises GA01 and GA03) using a two stage leach. *Biogeosciences Discussions*, 1-31. https://doi.org/10.5194/bg-2017-415

Shelley, R. U., Roca-Martí, M., Castrillejo, M., Sanial, V., Masqué, P., Landing, W. M., van Beek, P., Planquette, H., & Sarthou, G. (2017b). Quantification of trace element atmospheric deposition fluxes to the Atlantic Ocean (>40°N; GEOVIDE, GEOTRACES GA01) during spring 2014. *Deep Sea Research Part I: Oceanographic Research Papers*, *119*, 34-49. https://doi.org/https://doi.org/10.1016/j.dsr.2016.11.010

Sholkovitz, E. R., Sedwick, P. N., & Church, T. M. (2009). Influence of anthropogenic combustion emissions on the deposition of soluble aerosol iron to the ocean: Empirical estimates for island sites in the North Atlantic. *Geochimica et Cosmochimica Acta*, *73*(14), 3981-4003. https://doi.org/10.1016/j.gca.2009.04.029

Sholkovitz, E. R., Sedwick, P. N., Church, T. M., Baker, A. R., & Powell, C. F. (2012). Fractional solubility of aerosol iron: Synthesis of a global-scale data set. *Geochimica et Cosmochimica Acta*, *89*, 173-189. https://doi.org/https://doi.org/10.1016/j.gca.2012.04.022

Siegel, D. A., & Deuser, W. G. (1997). Trajectories of sinking particles in the Sargasso Sea: modeling of statistical funnels above deep-ocean sediment traps. *Deep Sea Research Part I: Oceanographic Research Papers*, *44*(9), 1519-1541. https://doi.org/https://doi.org/10.1016/S0967-0637(97)00028-9

Siegel, D. A., Fields, E., & Buesseler, K. O. (2008). A bottom-up view of the biological pump: Modeling source funnels above ocean sediment traps. *Deep Sea Research Part I: Oceanographic Research Papers*, *55*(1), 108-127. https://doi.org/https://doi.org/10.1016/j.dsr.2007.10.006

Smetacek, V., Klaas, C., Strass, V. H., Assmy, P., Montresor, M., Cisewski, B., Savoye, N., Webb, A., D'Ovidio, F., Arrieta, J. M., Bathmann, U., Bellerby, R., Berg, G. M., Croot, P., Gonzalez, S., Henjes, J., Herndl, G. J., Hoffmann, L. J., Leach, H., Losch, M., Mills, M. M., Neill, C., Peeken, I., Röttgers, R., Sachs, O., Sauter, E., Schmidt, M. M., Schwarz, J., Terbrüggen, A., & Wolf-Gladrow, D. (2012). Deep carbon export from a Southern Ocean iron-fertilized diatom bloom [Article]. *Nature*, *487*(7407), 313-319. https://doi.org/10.1038/nature11229

Streibel, T., Schnelle-Kreis, J., Czech, H., Harndorf, H., Jakobi, G., Jokiniemi, J., Karg, E., Lintelmann, J., Matuschek, G., Michalke, B., Muller, L., Orasche, J., Passig, J., Radischat, C., Rabe, R., Reda, A., Ruger, C., Schwemer, T., Sippula, O., Stengel, B., Sklorz, M., Torvela, T., Weggler, B., & Zimmermann, R. (2017). Aerosol emissions of a ship diesel engine operated with diesel fuel or heavy fuel oil. *Environ Sci Pollut Res Int*, *24*(12), 10976-10991. https://doi.org/10.1007/s11356-016-6724-z

Strzelec, M., Proemse, B. C., Barmuta, L. A., Gault-Ringold, M., Desservettaz, M., Boyd, P. W., Perron, M. M. G., Schofield, R., & Bowie, A. R. (2020). Atmospheric Trace Metal Deposition from Natural and Anthropogenic Sources in Western Australia. *Atmosphere*, *11*(5). https://doi.org/10.3390/atmos11050474

Suess, E., & Ungerer, C. (1981). Element and phase-composition of particulate matter from the circumpolar current between new-zealand and antarctica. *Oceanologica Acta*, *4*(2), 151-160.

Tagliabue, A., Aumont, O., & Bopp, L. (2014). The impact of different external sources of iron on the global carbon cycle. *Geophysical Research Letters*, *41*(3), 920-926. https://doi.org/10.1002/2013GL059059

Tagliabue, A., Bopp, L., Dutay, J.-C., Bowie, A. R., Chever, F., Jean-Baptiste, P., Bucciarelli, E., Lannuzel, D., Remenyi, T., Sarthou, G., Aumont, O., Gehlen, M., & Jeandel, C. (2010). Hydrothermal contribution to the oceanic dissolved iron inventory. *Nature Geoscience*, *3*(4), 252-256. https://doi.org/10.1038/ngeo818

Tagliabue, A., Bowie, A. R., Boyd, P. W., Buck, K. N., Johnson, K. S., & Saito, M. A. (2017). The integral role of iron in ocean biogeochemistry. *Nature*, *543*(7643), 51-59. https://doi.org/10.1038/nature21058

Tagliabue, A., Bowie, A. R., DeVries, T., Ellwood, M. J., Landing, W. M., Milne, A., Ohnemus, D. C., Twining, B. S., & Boyd, P. W. (2019). The interplay between regeneration and scavenging fluxes drives ocean iron cycling. *Nature Communications*, *10*(1), 4960. https://doi.org/10.1038/s41467-019-12775-5

Taylor, M. P. (2015). Atmospherically deposited trace metals from bulk mineral concentrate port operations. *Science of the Total Environment*, *515-516*, 143-152. https://doi.org/https://doi.org/10.1016/j.scitotenv.2015.02.010

Trull, T. W., Bray, S. G., Manganini, S. J., Honjo, S., & François, R. (2001). Moored sediment trap measurements of carbon export in the Subantarctic and Polar Frontal zones of the Southern Ocean, south of Australia. *Journal of Geophysical Research: Oceans*, *106*(C12), 31489-31509. https://doi.org/10.1029/2000JC000308

Trull, T. W., Jansen, P., Schulz, E., Weeding, B., Davies, D. M., & Bray, S. G. (2019). Autonomous Multi-Trophic Observations of Productivity and Export at the Australian Southern Ocean Time Series (SOTS) Reveal Sequential Mechanisms of Physical-Biological Coupling [10.3389/fmars.2019.00525]. *Frontiers in Marine Science*, *6*, 525. https://www.frontiersin.org/article/10.3389/fmars.2019.00525

Twining, B. S., & Baines, S. B. (2013). The Trace Metal Composition of Marine Phytoplankton. In C. A. Carlson & S. J. Giovannoni (Eds.), *Annual Review of Marine Science, Vol 5* (Vol. 5, pp. 191-215). https://doi.org/10.1146/annurev-marine-121211-172322

Wefer, G., & Fischer, G. (1993). Seasonal patterns of vertical particle flux in equatorial and coastal upwelling areas of the eastern Atlantic. *Deep Sea Research Part I: Oceanographic Research Papers*, *40*(8), 1613-1645. https://doi.org/https://doi.org/10.1016/0967-0637(93)90019-Y

Wilks, J. V., Rigual-Hernández, A. S., Trull, T. W., Bray, S. G., Flores, J.-A., & Armand, L. K. (2017). Biogeochemical flux and phytoplankton succession: A year-long sediment trap record in the Australian sector of the Subantarctic Zone. *Deep Sea Research Part I: Oceanographic Research Papers*, *121*, 143-159. https://doi.org/https://doi.org/10.1016/j.dsr.2017.01.001

Wynn-Edwards, C. A., Shadwick, E. H., Davies, D. M., Bray, S. G., Jansen, P., Trinh, R., & Trull, T. W. (2020). Particle Fluxes at the Australian Southern Ocean Time Series (SOTS) Achieve Organic Carbon Sequestration at Rates Close to the Global Median, Are Dominated by Biogenic Carbonates, and Show No Temporal Trends Over 20-Years [10.3389/feart.2020.00329]. *Frontiers in Earth Science*, *8*, 329. https://www.frontiersin.org/article/10.3389/feart.2020.00329

Yu, E. F., Francois, R., Bacon, M. P., Honjo, S., Fleer, A. P., Manganini, S. J., Rutgers Van Der Loeff, M. M., & Ittekot, V. (2001). Trapping efficiency of bottom-tethered sediment traps estimated from the intercepted fluxes of 230Th and 230Pa [Article]. *Deep-Sea Research Part I: Oceanographic Research Papers*, *48*(3), 865-889. https://doi.org/10.1016/S0967-0637(00)00067-4

Yu, Y., & Ginoux, P. (2020). Assessing the contribution of ENSO and MJO to Australian dust activity based on satellite and ground-based observations. *Atmos. Chem. Phys. Discuss.*, *2020*, 1-31. https://doi.org/10.5194/acp-2020-1206

Appendix 1.

Concentration data for internal sediment reference TT1811 MC45, certified plankton reference material BCR-414, and internal digestion replication assessment using SOTS sediment samples in this study are provided below.

Table A1. Target analyte blank corrected concentrations (ppm) of TT1811 MC45* from digests performed in this study (Batch 1-4) and in house reference runs. Relative standard deviation (%) for batches analysed in this study given. Digest recoveries based off previous in-house sediment reference TT1811 MC45. In-house reference was performed in triplicate. Batch 2 TT1811 was run in triplicate dilution with the mean presented. LR: Low Resolution, MR: Medium Resolution, ID: Isotope dilution

Analyte	Batch 1	Batch 2 (triplicate mean)	Batch 3	Batch 4	All batches mean	All batches RSD (%)	Batches 2-4 RSD (%)	TT1811 triplicate mean	TT1811 triplicate RSD (%)	Mean Recovery relative to TT1811	% Difference
Sr88(LR)	1686.17	1398.77	1402.45	1455.05	1456.66	7.88	1.83	1517.72	6.06	95.98	4.02
Y89(LR)	13.73	11.56	11.43	11.80	11.94	7.47	1.52	12.15	4.98	98.27	1.73
Mo95(LR)	0.63	0.55	0.52	0.52	0.55	7.17	2.86	0.51	9.78	108.58	8.58
Mo98(LR)	0.60	0.51	0.52	0.52	0.53	6.67	1.25				
Ag107(LR)	0.03	0.02	0.02	0.04	0.02	37.80	39.39	0.03	88.61	77.55	22.45
Ag109(LR)	0.03	0.02	0.01	0.04	0.02	42.37	45.29	0.02	96.03	141.73	41.73
Cd111(LR)	0.36	0.32	0.28	0.36	0.33	9.44	9.28	0.36	6.64	90.83	9.17
Cs133(LR)	0.15	0.12	0.13	0.13	0.13	10.44	5.87	0.12	23.09	111.35	11.35
Ba137(LR)	757.94	652.18	660.97	677.75	675.53	6.24	2.07	732.56	5.37	92.22	7.78
Ba138(LR)	764.68	663.61	665.34	691.12	685.33	5.98	2.17				
La139(LR)	6.81	5.82	5.66	5.97	5.98	7.02	2.23				
Ce140(LR)	7.24	6.25	6.18	6.41	6.43	6.31	1.51				
Nd146(LR)	6.18	5.35	5.30	5.47	5.50	6.19	1.40	5.19	4.98	105.91	5.91
Tm169(LR)	0.17	0.14	0.14	0.14	0.14	7.62	1.92	0.13	17.03	111.34	11.34
Yb171(LR)	1.03	0.91	0.87	0.94	0.93	6.02	2.91	0.84	9.64	110.00	10.00
Re185(LR)	0.02	-0.01	0.00	0.00	0.00	NA	NA				
Re187(LR)	0.02	-0.01	0.00	0.00	0.00	NA	NA				
Tl205(LR)	0.06	0.05	0.05	0.05	0.05	8.60	3.22	0.04	29.00	117.41	17.41
Pb208(LR)	10.98	9.27	8.99	9.41	9.53	7.59	1.73	8.62	4.71	110.65	10.65
Th230(LR)	0.33	0.30	0.29	0.30	0.30	4.51	2.20				
Th232(LR)	0.52	0.48	0.45	0.48	0.48	4.82	3.10	0.42	13.27	114.88	14.88
Th232(ID)	0.33	0.13	0.17	0.14	0.30	4.51	2.20				
U236(LR)	0.32	0.30	0.29	0.28	0.30	4.58	2.10				
U238(LR)	0.29	0.27	0.25	0.26	0.27	4.83	2.74	0.26	16.60	101.06	1.06
Na23(MR)	14766.65	12421.21	11011.84	12122.09	12527.37	10.00	5.61	11300.30	2.71	110.86	10.86
Mg24(MR)	3733.87	3225.60	3062.37	3179.74	3275.46	7.27	2.80	2887.98	3.37	113.42	13.42
Al27(MR)	6615.61	5604.84	5442.40	5705.79	5763.05	7.57	2.52	5576.17	4.64	103.35	3.35
P31(MR)	478.02	408.36	381.61	419.43	417.36	7.80	3.68	443.21	9.68	94.17	5.83
S32(MR)	1762.90	1444.10	1258.25	1375.52	1454.83	11.54	5.91	1515.27	3.93	96.01	3.99
Ca42(MR)	400564.19	321543.07	312241.46	321746.34	333196.87	9.99	1.53	316905.36	10.16	105.14	5.14
Sc45(MR)	2.57	2.27	2.23	2.23	2.31	5.82	1.75	2.23	7.82	103.53	3.53
Ti47(MR)	723.29	676.95	654.35	667.72	679.37	3.60	1.93	648.61	4.67	104.74	4.74
Ti49(MR)	750.00	674.35	642.34	667.81	680.53	5.36	2.22				
V51(MR)	27.56	24.68	24.33	24.55	25.08	4.96	1.17	23.59	7.09	106.30	1.06
Cr52(MR)	4.32	4.13	3.65	3.53	3.98	8.02	7.81	3.70	10.04	107.67	1.08
Mn55(MR)	1441.16	1288.45	1257.85	1321.02	1314.23	5.26	2.63	1283.18	7.73	102.42	1.02
Fe56(MR)	**8898.08**	**7992.69**	**7571.06**	**8220.44**	**8111.27**	**5.44**	**3.01**	**7763.74**	**7.82**	**104.48**	**1.04**
Co59(MR)	5.91	5.31	5.15	5.11	5.35	5.40	2.02	5.35	2.63	100.04	1.00
Ni60(MR)	16.30	13.93	13.49	13.67	14.21	7.38	1.73	13.40	5.80	106.00	1.06
Cu63(MR)	36.48	24.90	23.85	25.82	26.81	17.87	3.13	24.08	3.56	111.31	1.11
Zn66(MR)	26.86	17.94	16.70	20.97	19.72	19.18	8.83	16.10	4.91	122.50	1.22
Zn68(MR)	26.80	18.77	16.86	19.69	19.95	17.62	6.23				
Mean all analytes						9.35	5.08		13.95	105.80	7.66
Mean Al, Ti, Fe						5.54	2.49		5.71	104.19	3.05

*TT1811 MC45: Core sediment from CROCCA-2S cruise. Sediment origin from South Indian Ocean.

Table A2. Blank corrected concentration data (ppm) for certified plankton reference BCR-414 used in batches 1 and 2. Batches 3 and 4 did not include BCR-414, however high analytical precision was observed in batches 2-4 from internal reference TT1811 (Table S1). Recoveries are shown for the mean of all BCR-414 runs (n = 4). LR: Low Resolution, MR: Medium Resolution, ID: Isotope dilution

	BCR Batch 1	BCR-414-2.1	BCR-414-2.3	BCR-414-2.3	Mean Batch 2	% Change B1 to B2	BCR-414 Certified	BCR-414 indicative	Recovery relative to certified/ indicates
Sr88(LR)	247.02	224.79	226.84	225.21	225.61	-9.49		261±25	88.49
Y89(LR)	0.71	0.65	0.66	0.66	0.66	-7.66			
Mo95(LR)	1.18	1.32	1.32	1.31	1.31	10.19		1.35±0.20	94.83
Mo98(LR)	1.18	1.31	1.32	1.29	1.30	9.65			
Ag107(LR)	0.05	0.04	0.04	0.04	0.04	-19.03			
Ag109(LR)	0.05	0.05	0.04	0.04	0.04	-13.65			
Cd111(LR)	0.35	0.33	0.34	0.32	0.33	-5.14			
Cs133(LR)	0.44	0.28	0.28	0.27	0.28	-59.39			
Ba137(LR)	25.49	26.26	27.30	26.37	26.64	4.32			
Ba138(LR)	24.71	25.86	26.85	26.69	26.46	6.63			
La139(LR)	0.84	0.90	0.91	0.90	0.90	7.22			
Ce140(LR)	1.72	1.83	1.84	1.83	1.83	5.83			
Nd146(LR)	0.78	0.85	0.85	0.83	0.84	7.05			
Tm169(LR)	0.01	0.01	0.01	0.01	0.01	-5.09			
Yb171(LR)	0.06	0.06	0.06	0.06	0.06	-7.96			
Re185(LR)	0.01	0.00	0.00	-0.01	0.00	407.57			
Re187(LR)	0.01	0.00	0.00	0.00	0.00	426.47			
Tl205(LR)	0.03	0.04	0.04	0.04	0.04	14.88			
Pb208(LR)	3.70	3.67	3.71	3.65	3.68	-0.60	3.97±0.19		92.78
Th230(LR)	0.24	0.24	0.24	0.25	0.24	3.52			
Th232(LR)	0.35	0.41	0.41	0.40	0.40	12.72			
Th232(ID)	0.24	0.24	0.24	0.25	0.24	3.52			
U236(LR)	0.13	0.13	0.13	0.13	0.13	2.87			
U238(LR)	0.11	0.12	0.12	0.12	0.12	11.42			
Na23(MR)	8453.80	7857.25	7678.81	7939.04	7825.04	-8.04			
Mg24(MR)	2396.23	2340.58	2285.22	2279.37	2301.72	-4.11			
Al27(MR)	2119.84	2394.80	2297.11	2362.58	2351.50	9.85			
P31(MR)	13680.48	12293.11	12328.41	12036.85	12219.46	-11.96			
S32(MR)	6042.90	5525.57	5535.91	5505.32	5522.27	-9.43			
Ca42(MR)	67729.04	61339.32	60312.07	60470.37	60707.25	-11.57			
Sc45(MR)	0.40	0.46	0.48	0.48	0.47	14.52		0.54±0.02	84.15
Ti47(MR)	83.16	73.29	72.30	70.69	72.09	-15.35			
Ti49(MR)	67.30	71.96	68.28	69.66	69.97	3.81			
V51(MR)	8.46	8.63	8.32	8.61	8.52	0.72	8.1±0.18		105.00
Cr52(MR)	19.77	20.96	20.48	21.03	20.83	5.05	23.8±1.2		86.40
Mn55(MR)	271.02	256.78	252.69	255.18	254.88	-6.33	299±13		86.59
Fe56(MR)	**1670.34**	**1736.12**	**1705.10**	**1685.21**	**1708.81**	**2.25**		**1850±0.19**	**91.85**
Co59(MR)	1.32	1.30	1.32	1.38	1.33	0.75		1.43±0.06	93.16
Ni60(MR)	16.39	16.05	15.99	15.52	15.85	-3.41	18.8±0.8		85.04
Cu63(MR)	29.01	26.46	26.82	26.64	26.64	-8.88	29.5±1.3		92.31
Zn66(MR)	91.67	89.76	89.71	90.75	90.07	-1.77	111.6±2.5		81.07
Zn68(MR)	93.91	90.61	90.62	91.16	90.80	-3.42			
								Average all	90.14
								Average recovery from certified	89.88
								Average recovery from indicative	90.50

Table A3. Blank corrected concentration data (ppm) for five SOTS sample digest replicates across batches 1 and 2 to test digestion repeatability. % change from batch 1 to 2 is shown for each paired sample repeat analysis (negative = increase in concentration, positive indicates decrease in concentration in batch 2. RSD between batch 1 and 2 is shown, with the average RSD (%) across all 5 replicates also given. LR: Low Resolution, MR: Medium Resolution, ID: Isotope dilution

	Sample 1 digest 1	Sample 1 digest 2	% Change sample 1	RSD (%) Sample 1	Sample 2 digest 1	Sample 2 digest 2	% Change sample 2	RSD (%) Sample 2	Sample 3 digest 1	Sample 3 digest 2	% Change Sample 3	RSD (%) Sample 3
Sr88(LR)	1294.10	1280.71	-1.03	0.74	1407.23	1292.81	11.17	5.99	1202.97	1213.50	2.46	0.62
Y89(LR)	1.62	1.62	-0.36	0.25	1.84	1.61	12.17	9.33	2.02	2.01	3.46	0.54
Mo95(LR)	0.46	0.42	-9.49	7.04	0.42	0.34	13.17	14.76	3.34	3.21	4.46	2.77
Mo98(LR)	0.46	0.41	-10.94	8.18	0.42	0.33	14.17	16.03	3.41	3.20	5.46	4.52
Ag107(LR)	0.63	0.68	7.30	4.98	0.75	0.66	15.17	9.12	0.49	0.52	6.46	4.46
Ag109(LR)	0.62	0.64	3.32	2.31	0.73	0.65	16.17	7.67	0.49	0.50	7.46	1.55
Cd111(LR)	2.52	2.51	-0.48	0.34	2.54	2.35	17.17	5.58	2.68	2.80	8.46	3.24
Cs133(LR)	0.09	0.07	-19.88	15.61	0.05	0.04	18.17	19.46	0.14	0.14	9.46	4.80
Ba137(LR)	1023.83	986.00	-3.69	2.66	1013.58	916.66	19.17	7.10	1186.31	1155.56	10.46	1.86
Ba138(LR)	1025.46	1009.88	-1.52	1.08	1021.46	932.89	20.17	6.41	1200.29	1172.32	11.46	1.67
La139(LR)	1.12	1.10	-1.82	1.30	1.23	1.02	21.17	13.27	1.24	1.23	12.46	0.81
Ce140(LR)	1.61	1.55	-3.78	2.72	1.59	1.26	22.17	16.55	2.07	2.03	13.46	1.14
Nd146(LR)	1.02	1.02	0.01	0.01	1.13	0.92	23.17	14.22	1.14	1.07	14.46	4.18
Tm169(LR)	0.02	0.02	-12.57	9.49	0.02	0.02	24.17	16.37	0.03	0.02	15.46	8.15
Yb171(LR)	0.13	0.13	0.72	0.50	0.14	0.13	25.17	6.04	0.19	0.18	16.46	3.97
Re185(LR)	0.03	-0.01	-122.03	221.33	0.02	-0.01	26.17	247.81	0.00	-0.01	17.46	-289.09
Re187(LR)	0.03	-0.01	-125.09	236.15	0.02	-0.01	27.17	248.29	0.00	-0.01	18.46	-275.79
Tl205(LR)	0.02	0.01	-30.14	25.10	0.02	0.01	28.17	41.32	0.03	0.03	19.46	2.69
Pb208(LR)	1.35	1.31	-3.37	2.43	1.33	1.03	29.17	18.30	2.36	2.26	20.46	3.10
Th232 - ID	0.12	0.11	-7.87	5.79	0.11	0.09	30.17	13.43	0.17	0.17	21.46	3.39
Th232(LR)	0.20	0.17	-15.52	11.89	0.18	0.12	31.17	25.05	0.29	0.25	22.46	12.15
U238 - ID	0.24	0.24	-0.18	0.13	0.22	0.20	33.17	6.22	0.34	0.33	24.46	0.63
U238(LR)	0.21	0.20	-2.67	1.92	0.20	0.16	34.17	16.53	0.32	0.28	25.46	7.78
Na23(MR)	1835.76	1715.54	-6.55	4.79	1576.39	1374.80	36.17	9.66	4801.18	4375.60	27.46	6.56
Mg24(MR)	1739.22	1795.90	3.26	2.27	1463.72	1405.38	37.17	2.88	3043.04	3031.26	28.46	0.27
Al27(MR)	1216.35	1133.18	-6.84	5.01	826.22	757.52	38.17	6.13	1947.97	1849.86	29.46	3.65
P31(MR)	1188.55	1286.37	8.23	5.59	1150.43	1119.22	39.17	1.94	1479.19	1519.26	30.46	1.89
S32(MR)	2664.70	2568.73	-3.60	2.59	2441.56	2196.88	40.17	7.46	4660.34	4442.27	31.46	3.39
Ca42(MR)	257839.76	262059.24	1.64	1.15	303205.35	289425.62	41.17	3.29	282559.61	264278.87	32.46	4.73
Sc45(MR)	0.25	0.27	6.37	4.36	0.24	0.24	42.17	0.84	0.36	0.34	33.46	3.47
Ti47(MR)	40.24	40.35	0.28	0.20	30.05	26.03	43.17	10.12	64.88	66.70	34.46	1.95
Ti49(MR)	39.93	42.67	6.86	4.69	27.78	27.25	44.17	1.36	69.43	67.48	35.46	2.02
V51(MR)	2.97	3.06	3.07	2.14	2.39	2.16	45.17	7.12	4.10	4.05	36.46	0.81
Cr52(MR)	1.97	1.95	-1.25	0.89	1.93	1.46	46.17	19.39	3.42	3.53	37.46	2.21
Mn55(MR)	5.06	3.38	-33.18	28.13	3.12	0.75	47.17	86.56	15.17	12.93	38.46	11.30
Fe56(MR)	726.39	675.19	-7.05	5.17	461.42	406.02	48.17	9.03	1088.68	1051.55	39.46	2.45
Co59(MR)	0.30	0.30	-0.34	0.24	0.25	0.24	49.17	3.81	0.75	0.80	40.46	4.58
Ni60(MR)	9.44	9.12	-3.39	2.44	8.81	7.52	50.17	11.18	18.89	18.47	41.46	1.58
Cu63(MR)	16.21	16.42	1.29	0.90	16.52	14.60	51.17	8.72	24.81	24.61	42.46	0.56
Zn66(MR)	86.91	90.97	4.67	3.22	110.44	104.42	52.17	3.96	87.28	89.49	43.46	1.77
Zn68(MR)	89.25	89.52	0.31	0.22	109.34	105.11	53.17	2.79	88.81	89.59	44.46	0.62

Table A3. continued

	Sample 4 digest 1	Sample 4 digest 2	% Change sample 4	RSD (%) Sample 4	Sample 5 digest 1	Sample 5 digest 1	% Change sample 5	RSD (%) Sample 5	1-5 Mean change %	1-5 Mean RSD (%)
Sr88(LR)	1427.00	1437.12	2.62	0.50	1304.84	1370.46	-1.56	3.47	2.73	2.26
Y89(LR)	2.14	2.20	3.62	1.75	1.98	2.07	-0.56	2.94	3.66	2.96
Mo95(LR)	0.73	0.72	4.62	0.97	0.71	0.69	0.44	2.77	2.64	5.66
Mo98(LR)	0.73	0.70	5.62	2.14	0.74	0.73	1.44	0.36	3.15	6.25
Ag107(LR)	0.34	0.36	6.62	4.05	0.31	0.33	2.44	5.63	7.60	5.65
Ag109(LR)	0.33	0.35	7.62	5.14	0.31	0.32	3.44	2.58	7.60	3.85
Cd111(LR)	5.17	5.32	8.62	1.90	3.34	3.58	4.44	4.85	7.64	3.18
Cs133(LR)	0.16	0.15	9.62	3.04	0.12	0.12	5.44	0.82	4.56	8.75
Ba137(LR)	1107.84	1057.99	10.62	3.25	941.85	938.15	6.44	0.28	8.60	3.03
Ba138(LR)	1107.16	1090.84	11.62	1.05	948.03	962.71	7.44	1.09	9.83	2.26
La139(LR)	1.44	1.42	12.62	1.21	1.34	1.34	8.44	0.00	10.57	3.32
Ce140(LR)	1.92	1.81	13.62	4.38	1.59	1.61	9.44	1.02	10.98	5.16
Nd146(LR)	1.30	1.19	14.62	6.20	1.15	1.11	10.44	1.99	12.54	5.32
Tm169(LR)	0.02	0.02	15.62	2.19	0.02	0.02	11.44	7.71	10.82	8.78
Yb171(LR)	0.16	0.17	16.62	1.40	0.16	0.16	12.44	0.91	14.28	2.56
Re185(LR)	0.02	-0.01	17.62	451.12	0.04	-0.01	13.44	235.83	-9.47	173.40
Re187(LR)	0.02	-0.01	18.62	419.95	0.03	-0.01	14.44	250.07	-9.28	175.74
Tl205(LR)	0.04	0.03	19.62	6.96	0.03	0.03	15.44	5.33	10.51	16.28
Pb208(LR)	2.30	2.10	20.62	6.45	1.87	1.70	16.44	6.67	16.66	7.39
Th232 - ID	**0.17**	**NA**	**NA**	**NA**	**0.14**	**0.15**	**17.44**	**1.57**	**12.24**	**6.04**
Th232(LR)	0.29	0.25	22.62	9.53	0.25	0.21	18.44	10.22	15.83	13.77
U238 - ID	0.41	0.41	24.62	0.19	0.66	0.70	20.44	3.68	20.50	2.17
U238(LR)	0.39	0.35	25.62	6.58	0.61	0.57	21.44	4.15	20.80	7.39
Na23(MR)	2297.12	2086.01	27.62	6.81	3334.57	3214.77	23.44	2.59	21.63	6.08
Mg24(MR)	2665.66	2615.30	28.62	1.35	2642.88	2761.16	24.44	3.10	24.39	1.97
Al27(MR)	**2350.74**	**2194.57**	**29.62**	**4.86**	**1952.87**	**1875.52**	**25.44**	**2.86**	**23.17**	**4.50**
P31(MR)	1452.09	1477.36	30.62	1.22	1452.80	1859.25	26.44	17.36	26.98	5.60
S32(MR)	3934.17	3694.76	31.62	4.44	3777.19	3764.18	27.44	0.24	25.42	3.62
Ca42(MR)	284165.10	283102.38	32.62	0.26	258667.09	257369.20	28.44	0.36	27.26	1.96
Sc45(MR)	0.45	0.47	33.62	2.33	0.44	0.45	29.44	1.41	29.01	2.48
Ti47(MR)	**61.13**	**70.05**	**34.62**	**9.61**	**51.89**	**57.24**	**30.44**	**6.94**	**28.59**	**5.77**
Ti49(MR)	65.29	75.95	35.62	10.67	51.42	62.62	31.44	13.90	30.71	6.53
V51(MR)	4.68	4.40	36.62	4.40	4.82	4.90	32.44	1.15	30.75	3.12
Cr52(MR)	3.56	3.72	37.62	3.19	2.76	2.88	33.44	2.95	30.69	5.73
Mn55(MR)	12.52	10.25	38.62	14.11	10.47	8.41	34.44	15.43	25.10	31.11
Fe56(MR)	**1285.01**	**1207.81**	**39.62**	**4.38**	**956.03**	**941.26**	**35.44**	**1.10**	**31.13**	**4.43**
Co59(MR)	0.71	0.74	40.62	2.96	0.58	0.52	36.44	6.81	33.27	3.68
Ni60(MR)	12.28	11.46	41.62	4.87	10.76	10.46	37.44	1.98	33.46	4.41
Cu63(MR)	17.22	16.78	42.62	1.83	15.65	16.34	38.44	3.05	35.19	3.01
Zn66(MR)	56.63	55.23	43.62	1.77	45.91	47.67	39.44	2.65	36.67	2.68
Zn68(MR)	55.40	55.91	44.62	0.66	45.69	46.93	40.44	1.89	36.60	1.23